PNAS RESEARCH ARTICLE | APPLIED PHYSICAL SCIENCES

Interfacial Cherenkov radiation from ultralow-energy electrons

Zheng Gong[a,b], Jialin Chen[a,b,c], Ruoxi Chen[a,b], Xingjian Zhu[d], Chan Wang[a,e], Xinyan Zhang[a,b], Hao Hu[f], Yi Yang[g], Baile Zhang[h,i,1], Hongsheng Chen[a,b,e,j,1], Ido Kaminer[c], and Xiao Lin[a,b,1]

Edited by Hui Cao, Yale University, New Haven, CT; received April 23, 2023; accepted August 11, 2023

Cherenkov radiation occurs only when a charged particle moves with a velocity exceeding the phase velocity of light in that matter. This radiation mechanism creates directional light emission at a wide range of frequencies and could facilitate the development of on-chip light sources except for the hard-to-satisfy requirement for high-energy particles. Creating Cherenkov radiation from low-energy electrons that has no momentum mismatch with light in free space is still a long-standing challenge. Here, we report a mechanism to overcome this challenge by exploiting a combined effect of interfacial Cherenkov radiation and umklapp scattering, namely the constructive interference of light emission from sequential particle–interface interactions with specially designed (umklapp) momentum-shifts. We find that this combined effect is able to create the interfacial Cherenkov radiation from ultralow-energy electrons, with kinetic energies down to the electron-volt scale. Due to the umklapp scattering for the excited high-momentum Bloch modes, the resulting interfacial Cherenkov radiation is uniquely featured with spatially separated apexes for its wave cone and group cone.

Cherenkov radiation | transition radiation | umklapp scattering | photonic crystals

Significance

Cherenkov radiation is fundamentally limited by Cherenkov threshold, since it generally originates from particle-bulk interactions. This fundamental limitation requires the usage of high-energy charged particles for its creation and impedes many promising applications, such as novel on-chip light sources. Recently, interfacial Cherenkov radiation was revealed by engineering the interference of light emission from sequential particle–interface interactions. Here we report the enticing capability of interface-effect-based Cherenkov radiation to overcome the fundamental limitation of Cherenkov threshold for conventional bulk-effect-based Cherenkov radiation. Remarkably, we find the possibility to create threshold-free interfacial Cherenkov radiation with the aid of umklapp scattering. Our work thus may pave the way toward compact on-chip light sources at some desired frequencies (e.g., terahertz or ultraviolet regimes) from low-energy electrons.

Cherenkov radiation (1–7) is a typical type of free-electron radiation that is crucial to many practical applications, ranging from Cherenkov detectors (8–13), light sources (14–16), and medical imaging (17–19), to photodynamic therapy (20–22). These applications are enabled by a unique feature of Cherenkov radiation, namely the capability to create light emission with high directionality at any frequency, given a charged particle moves with a velocity above the Cherenkov threshold (23, 24), which corresponds to the phase velocity of light in the background matter. As fundamentally restricted by the Cherenkov threshold, these applications have to rely on high-energy particles. For example, the kinetic energies of charged particles used in medical imaging and therapy is in the order of mega-electron-volts (MeV) (22); Cherenkov detectors are useful for the identification of high-energy particles generally in the order of giga-eV (GeV) (12, 13). There is a continuous quest to reduce the Cherenkov threshold, with the hope of even creating Cherenkov radiation from slow electrons. Achieving free-electron radiation (e.g., Cherenkov radiation) from slow electrons (16, 25–30) is now an active area of research that is highly sought after and is of special importance, especially for its prospects to boost the development of integrated light sources.

The reduction of Cherenkov threshold generally relies on the usage of high-momentum modes with low phase velocities, such as those in hyperbolic materials (16, 31–40). Such materials are fundamentally limited by losses and nonlocality (32–34). This way, the phase velocity of these hyperbolic modes cannot reduce to absolute zero; nevertheless, it can be orders of magnitude smaller than the speed of light in free space, leading to low-threshold Cherenkov radiation (16, 32). However, these hyperbolic modes, once excited, remain difficult to couple into free space, since they still suffer from severe momentum mismatch with light in free space and would be totally reflected at the material interface. To extract these hyperbolic modes into free space, additional structural design is mandatory, such as the tilting of the optical axis of hyperbolic materials (35), the nanopatterning of hyperbolic materials themselves (36, 37), or the addition of patterned nanostructures on the interface of hyperbolic materials (16, 38). These additional structural designs for outcoupling purposes may deteriorate the properties of originally excited Cherenkov radiation inside hyperbolic materials, such as the unique relation between the Cherenkov angle and the particle velocity, the directionality, and the radiation spectrum. In short, despite the long history of free-electron radiation (41–50), the creation of Cherenkov radiation that has no momentum mismatch with light in free space from slow electrons remains an enticing but challenging goal. Here, we propose a mechanism to achieve this goal using a unique combination: the umklapp scattering and the constructive interference of radiation from many parallel interfaces, namely transition radiation.

Author contributions: Z.G. and X.L. designed research; Z.G. performed research; Z.G., J.C., R.C., X. Zhu, C.W., X. Zhang, H.H., Y.Y., B.Z., H.C., I.K., and X.L. analyzed data; B.Z., H.C., I.K., and X.L. supervised the project; and Z.G. and X.L. wrote the paper.

The authors declare no competing interest.

This article is a PNAS Direct Submission.

[1]To whom correspondence may be addressed. Email: xiaolinzju@zju.edu.cn, hansomchen@zju.edu.cn, or blzhang@ntu.edu.sg.

This article contains supporting information online at https://www.pnas.org/lookup/suppl/doi:10.1073/pnas.2306601120/-/DCSupplemental.

Published September 11, 2023.

Transition radiation (51–54) originates from particle–interface interactions. It is distinct from the conventional bulk Cherenkov radiation originating from particle–bulk interactions. The conventional transition radiation could occur at any electron velocity and is of poor directionality, especially for slow electrons, but inherently momentum-matched with light in free space. Recently, we revealed in ref. 13 that the constructive interference of transition radiation excited by the interaction between relativistic charged particles and many parallel interfaces can effectively form an alternative type of Cherenkov radiation with high directionality. Since this type of effective Cherenkov radiation is induced by particle–interface interactions, we suggest to denote it as interfacial Cherenkov radiation, which intrinsically has no momentum mismatch with light in free space and can thus freely couple into free space. The study of interfacial Cherenkov radiation has already demonstrated its potential in the design of nanophotonic Cherenkov detectors for identifying high-energy particles (13) but is still in its infancy. Whether the interface effect could also be exploited to create the interfacial Cherenkov radiation from slow electrons remains an open question.

In this work, we reveal the possibility of creating interfacial Cherenkov radiation from ultralow-energy electrons. We find that the interfacial Cherenkov radiation is essentially threshold-free since the accompanied umklapp scattering could flexibly shift the momentum of excited high-momentum Bloch modes along the direction of periodicity. While high-momentum Bloch modes in photonic crystals (55–59) were used to reduce the Cherenkov threshold, previous works focused on the discussion of conventional bulk Cherenkov radiation inside photonic crystals (55). Since the umklapp scattering would reshape the wave cone (namely a constant-phase surface), we find that the interfacial Cherenkov radiation is also featured with spatially separated apexes for its wave cone and group cone (related to the crest of light emission or the Cherenkov cone).

We begin with the Huygens construction (60–62) for the wave and group cones of interfacial Cherenkov radiation inside an ideal unbounded 1D photonic crystal in Fig. 1 *A*–*F*. Without loss of generality, the photonic crystal is composed of two transparent dielectrics, such as those with relative permittivities of $\varepsilon_{r,1}$ and $\varepsilon_{r,2}$, respectively. In order to let the electrons safely pass through the photonic crystal, one may drill a tiny hole (14) through the photonic crystal along the electron trajectory. Generally, the Huygens construction for the wave and group cones of Cherenkov radiation is related to four types of velocities, namely the electron

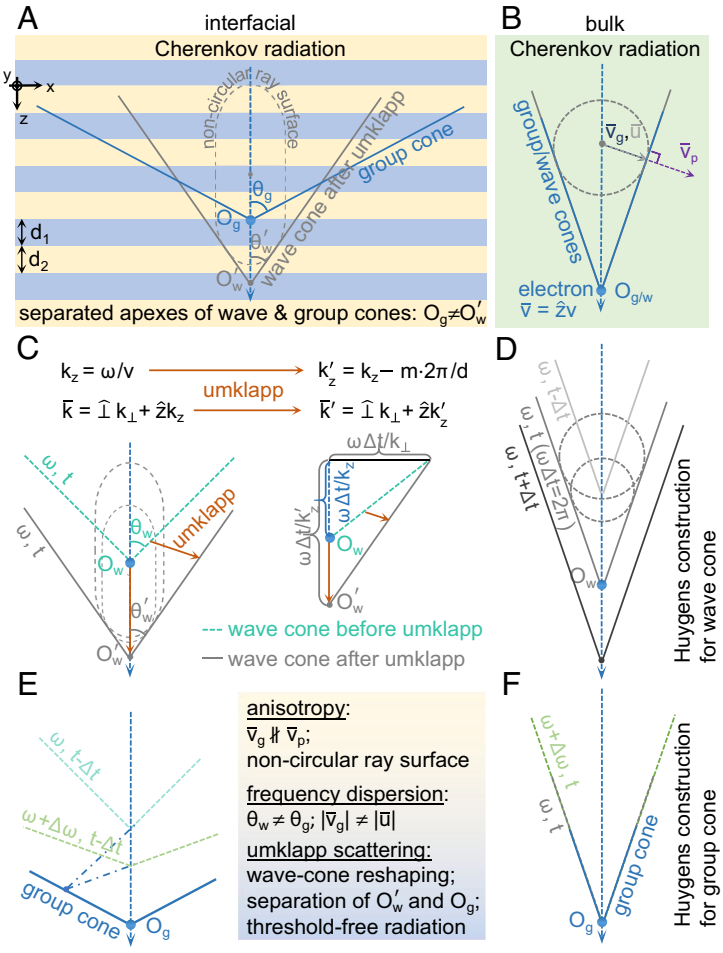

Fig. 1. Huygens construction of interfacial Cherenkov radiation with umklapp scattering inside an infinitely large one-dimensional photonic crystal. The photonic crystal is composed of two transparent materials with relative permittivities of $\varepsilon_{r,1}$ and $\varepsilon_{r,2}$ and thicknesses of d_1 and d_2, respectively. The Huygens construction of wave and group cones is related to four velocities, namely the electron velocity $\bar{v} = \hat{z}v$, the phase velocity $\bar{v}_p$, the group velocity $\bar{v}_g$, and the ray velocity $\bar{u}$. (*A*, *C*, and *E*) Interfacial Cherenkov radiation. (*B*, *D*, and *F*) Conventional bulk Cherenkov radiation inside an isotropic material without dispersion. The generatrix of the wave cone for monochromatic waves in *C* and *D* can be constructed by plotting the common tangent of Huygens wavelets with a same frequency ω emitted at different times. Since the monochromatic waves are radiated not in pulse, but continuously, there would be a series of wave cones whose generatrices are parallel to each other; see the instant positions of a series of wave cones with phase difference of $\omega\Delta t = 2\pi$ in *D*. The intersections of all wave-cone generatrices for two neighboring frequencies ω and $\omega + \Delta\omega$ would give the instant surface of equal phases for these two frequencies, namely the instant position of group cone in *E* and *F*, where $\Delta\omega/\omega \to 0$. From the causality principle, the apex of the group cone always coincides with the instant position of the moving electron. Due to the umklapp scattering, the wave cone would be reshaped, including its apex and aperture.

velocity $\overline{v} = \hat{z}v$, the group velocity $\overline{v}_g = \hat{\perp}v_{g,\perp} + \hat{z}v_{g,z}$, the phase velocity $\overline{v}_p = \hat{k}v_p = \hat{\perp}v_{p,\perp} + \hat{z}v_{p,z}$, and the ray velocity $\overline{u} = \hat{\perp}u_\perp + \hat{z}u_z$, where $\hat{\perp}$ is a basis vector perpendicular to the electron velocity. The electron's velocity would be below the Cherenkov threshold by imposing the constraint of $v < min\left(c/\sqrt{\varepsilon_{r,1}}, c/\sqrt{\varepsilon_{r,2}}\right)$ in Fig. 1 *A*, *C*, and *E*; as a result, the possibility of conventional bulk Cherenkov radiation inside the photonic crystal is excluded. The group velocity in this work maintains its physical meaning as the velocity of energy flow (63, 64), since there is no anomalous dispersion in our studied system. While the phase velocity $\overline{v}_p = \hat{k}v_p$ represents the velocity of phase propagation along the wavevector $\overline{k}$ of the emitted light, the ray velocity corresponds to the velocity of phase propagation along the ray, namely along the direction of energy flow (61, 62). Mathematically, we have $\hat{k} \cdot \overline{u} = v_p$ and $\overline{u} \| \overline{v}_g$ (60–62).

Due to the anisotropy of photonic crystals, the phase velocity and group velocity of Bloch modes are nonparallel, and a noncircular ray surface is formed for all Bloch modes and thus the secondary Huygens wavelets at a given frequency in Fig. 1*A*. With the knowledge of ray surface (60, 65), the wave cone with an aperture θ_w can be constructed by the common tangent of secondary Huygens wavelets in Fig. 1*C*, where $\theta_w = \arctan\left(\frac{u_\perp}{v-u_z}\right) = \arcsin\left(\frac{v_p}{v}\right)$ is related to either the ray or phase velocity (*SI Appendix*, section S3). Correspondingly, the intersection of all wave-cone generatrices for two neighboring frequencies would determine the instant position of the group cone with an aperture θ_g in Fig. 1*E*, where $\theta_g = \arctan\left(\frac{v_{g,\perp}}{v-v_{g,z}}\right)$ is related to the group velocity. Due to the frequency dispersion of photonic crystals, we generally have nonidentical magnitudes for the ray and group velocities, namely $|\overline{u}| \neq |\overline{v}_g|$. As a result, the apertures for the wave and group cones are generally not identical, namely $\theta_g \neq \theta_w$. Since these properties are purely induced by the anisotropy and the frequency dispersion, they are not unique to the interfacial Cherenkov radiation but in principle can occur for the conventional bulk Cherenkov radiation, for example, inside an anisotropic material with the presence of frequency dispersion (62, 66, 67). For comparison, we also show the Huygens construction for conventional bulk Cherenkov radiation inside an isotropic material with a relative permittivity of $\varepsilon_r = \varepsilon_{r,2}$ in Fig. 1 *B*, *D*, and *F*. Due to the isotropy and the absence of frequency dispersion, the bulk Cherenkov radiation has a circular ray surface for the secondary Huygens wavelets, $\overline{v}_p = \overline{v}_g = \overline{u}$, and $\theta_g = \theta_w$.

The interfacial Cherenkov radiation from low-energy electrons is always accompanied by the umklapp scattering due to the structural periodicity of photonic crystals. The umklapp scattering plays a critical role in reshaping the wave cone of interfacial Cherenkov radiation in Fig. 1*C*, including its aperture and apex. In the absence of the umklapp scattering, the emitted Bloch mode has a wavevector of $\overline{k} = \hat{\perp}k_\perp + \hat{z}k_z$, where $k_z = \omega/v$ is determined by the electron velocity according to the phase matching condition between the emitted light and the moving electron. Correspondingly, the original wave cone has an aperture of $\theta_w = \arcsin\left(\frac{v_p}{v}\right) = \arctan\left(\frac{k_z}{k_\perp}\right)$, and the apex of each wave cone moves with a velocity of $\overline{v}_{apex,w} = \frac{\hat{z}\omega}{k_z} = \hat{z}v = \overline{v}$. Since $\overline{v}_{apex,w}$ is equal to the electron velocity, the apex O_w of one specific wave cone could be spatially overlapped with the moving electron at any time. Due to the umklapp scattering along the periodicity direction, the z-component of wavevector would be changed from k_z to $k'_z = k_z - m \cdot 2\pi/d$, where d is the unit-cell thickness of photonic crystals and the Fourier order m is a nonzero integer. As a result, the excited Bloch mode after the umklapp scattering has a wavevector of $\overline{k}' = \hat{\perp}k_\perp + \hat{z}k'_z$. Then, each wave cone would be reshaped to have an aperture of $\theta'_w = \arctan\left(\frac{k'_z}{k_\perp}\right)$. Moreover, the apex of each wave cone would be reshaped to move with a velocity of $\overline{v}'_{apex,w} = \hat{z}\omega/k'_z$. Because $\overline{v}'_{apex,w} \neq \overline{v}$, the apexes of all wave cones would be spatially separated from the moving electron as the time varies. For example, the apex O_w is reshaped to O'_w, whose position is ahead of the moving electron in Fig. 1*C*. These modifications to the wave cone do not violate the causality principle (65) because the wave cone does not necessarily carry the radiated energy.

On the other hand, the group cone of interfacial Cherenkov radiation would not undergo the umklapp scattering, as fundamentally governed by the causality principle. Correspondingly, the Huygens construction of the group cone in Fig. 1*E* should use the original wave cones before the umklapp scattering. In other words, the apex of the group cone should always be spatially overlapped with the position of the moving electron and moves with a velocity of $\overline{v}_{apex,g} = \overline{v}$, since the group cone is related to the propagation of the radiated energy which emanates from the moving electron. While the interfacial Cherenkov radiation has $\overline{v}_{apex,g} \neq \overline{v}'_{apex,w}$, there exists no such a reshaped wave cone after the umklapp scattering whose apex is overlapped with that of the group cone at any time, namely $O_g \neq O'_w$.

To facilitate the understanding of interfacial Cherenkov radiation, we show the spatial distribution of excited fields when an electron moves inside an infinitely large photonic crystal in Fig. 2 *A* and *C* and an infinitely-large homogeneous material in Fig. 2 *B* and *D*. At the frequency domain, the field $D_z(\omega)$ is shown in Fig. 2 *A* and *B*. Plane-like waves are created inside both the photonic crystal and the homogeneous material, which represent a direct signature for the emergence of Cherenkov radiation. This way, Fig. 2 *A* and *B* indicate that the constructive interference of light emission from particle–interface interactions could offer an alternative way to create the Cherenkov radiation, in addition to particle–bulk interactions. At the time domain in Fig. 2 *C* and *D*, the field $D_z(t) = \int d\omega D_z(\omega) e^{-i\omega t} F_{win}(\omega)$ is calculated in Fig. 2 *C* and *D*, where a window function $F_{win}(\omega)$ is used to get a clear picture of the group cone. Since $\overline{v}_{apex,g} \neq \overline{v}'_{apex,w}$, the interfacial Cherenkov radiation in Fig. 2*C* has spatially separated apexes for its wave cone after the umklapp scattering and its group cone (namely $O_g \neq O'_w$), and it is distinct from the conventional bulk Cherenkov radiation ($O_g = O_w$) in Fig. 2*D*.

To consider the potential influence of reflection at the interface of photonic crystals, we further investigate the interfacial Cherenkov radiation from a photonic crystal with a finite length in Figs. 3 and 4. The photonic crystal is surrounded by free space, and it has a unit-cell number of 200 in Figs. 3 and 4. For the interfacial Cherenkov radiation, the corresponding momentum mismatch and the total internal reflection could be avoided by imposing the constraint of $|k_\perp| \leq k_0$, where k_0 is the wavevector of emitted light into free space. By enforcing the boundary conditions, we have the radiation angle $\theta = \arcsin\left(\frac{|k_\perp|}{k_0}\right)$, which is the angle between $\overline{k}$ and $\overline{v}$ ($-\overline{v}$) for the forward (backward) radiation as schematically shown in Fig. 3*A*. Under this scenario, we

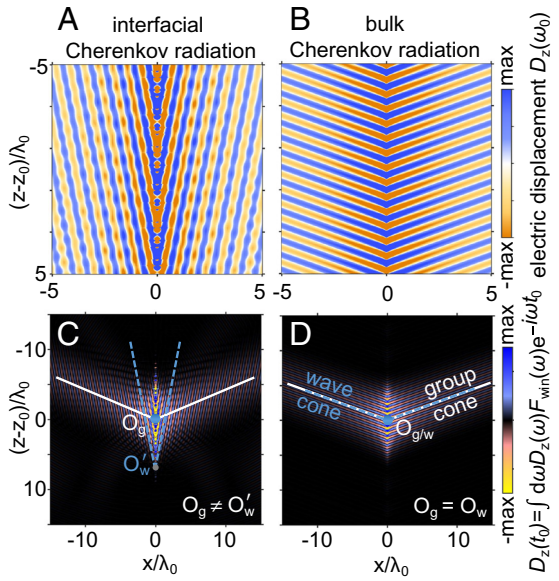

Fig. 2. Real-space demonstration of wave and group cones for interfacial Cherenkov radiation inside an infinitely large photonic crystal. The structural setup of the photonic crystal is $\varepsilon_{r,1} = 2.1$, $\varepsilon_{r,2} = 2.3$, $d_1 = 0.3\lambda_0$, and $d_2 = 0.7\lambda_0$, where λ_0 is working wavelength in free space. For the interfacial Cherenkov radiation in the left panel, the electron velocity of $v = 0.4c < \min\left(c/\sqrt{\varepsilon_{r,1}}, c/\sqrt{\varepsilon_{r,2}}\right)$ is used. That is, this electron velocity is chosen to be below the Cherenkov threshold and the corresponding kinetic energy is 46.5 keV. For the bulk Cherenkov radiation in the *Right* panel, an isotropic material with a relative permittivity of $\varepsilon_r = \varepsilon_{r,2}$ and the electron velocity of $v = 0.7c > c/\sqrt{\varepsilon_r}$ are used. That is, this electron velocity is chosen to be above the Cherenkov threshold and the corresponding kinetic energy is 205 keV. The instant position of the electron is at $z = z_0$ for the time of $t = t_0$. (*A* and *B*) Distribution of excited field $D_z(\omega_0)$. Plane-like waves are induced both for the interfacial and bulk Cherenkov radiation. (*C* and *D*) Distribution of excited field $D_z(t_0) = \int d\omega D_z(\omega) e^{-i\omega t_0} F_{win}(\omega)$, where a window function $F_{win}(\omega) = e^{-\frac{\sigma_z^2(\omega-\omega_0)^2}{2v^2}}$ with $\sigma_z = 2.5\lambda_0$ is used for the illustration of the group cone.

find the relationship between the electron velocity $\overline{v}$ and the radiation angle θ is governed by

$$v = \frac{\omega d}{2m\pi + \phi(\theta, \omega)} \quad [1]$$

$$\phi(\theta,\omega) = \arccos\left[\cos k_{z,1}d_1 \cos k_{z,2}d_2 - \frac{1}{2}\sin\left(k_{z,1}d_1\right)\right.$$
$$\left.\sin\left(k_{z,2}d_2\right)\left(\frac{\varepsilon_{r,1}k_{z,2}}{\varepsilon_{r,2}k_{z,1}} + \frac{\varepsilon_{r,2}k_{z,1}}{\varepsilon_{r,1}k_{z,2}}\right)\right] \quad [2]$$

where $d = d_1 + d_2$ is the unit-cell thickness of photonic crystals, d_j is the thickness of the photonic crystal constituent with $\varepsilon_{r,j}$, $k_{z,j} = k_0\sqrt{\varepsilon_{r,j} - \sin^2\theta}$, and j is either 1 or 2.

The factor of $2m\pi$ in Eq. **1** stems exactly from the umklapp scattering, whose existence ensures the possible solution of θ in Eq. **1** even under the scenario of $v/c \ll 1$, where c is the speed of light in free space. In other words, the interfacial Cherenkov radiation is in principle threshold-free, as can be seen from the dependence of the radiation angle on the electron velocity in Fig. 3 *B* and *C*. For example, the interfacial Cherenkov radiation could occur even when the electron velocity is down to the order of $10^{-2}c$ in Fig. 3*C*, due to the umklapp scattering with $m = 45$ for high-k Bloch modes (or down to the order of $10^{-3}c$ with $m = 900$ in *SI Appendix*, Fig. S8).

To rigorously demonstrate the angular feature of interfacial Cherenkov radiation, its total angular spectral energy density $U_{\text{total}}(\theta, v)$ is shown in Fig. 3*D* by following and extending Ginzburg and Frank's theory of transition radiation within the framework of classic electromagnetic wave theory (13, 51, 52, 68–72). In principle, our results do not depend on the specific choice of working angular frequency ω, as long as the emitted photon energy $\hbar\,\hbar\omega$ is much smaller than the kinetic energy E_k of electrons, namely $\hbar\,\hbar\omega \ll E_k$, so that the quantum recoil effect (48) can be safely neglected. The interfacial Cherenkov radiation with high directionality from ultralow-energy electrons manifests itself as the radiation peaks in the θ -v parameter space. Moreover, the trajectory of these radiation peaks in Fig. 3*D* is in accordance with the relationship between θ and v as revealed in Fig. 3*C*, which proves the validity of Eq. **1**. On the other hand, there are regions in the θ–v parameter space with the absence of interfacial Cherenkov radiation in Fig. 3 *B* and *D*. This is due to the failure of forming the constructive interference of light emission from particle–interface interactions. This way, the free-electron radiation in these regions still behaves as the conventional transition radiation and suffers from the low directionality and the low intensity in Fig. 3*D*.

Moreover, we find that the interfacial Cherenkov radiation has a certain tolerance to the variation of material's permittivity in *SI Appendix*, Fig. S4, the variation of the thickness of each constituent dielectric layer in *SI Appendix*, Fig. S5, and the material loss in *SI Appendix*, Fig. S6. Meanwhile, the photon extraction efficiency (26, 70) of interfacial Cherenkov radiation would exhibit a periodic oscillation tendency with respect to the order of umklapp scattering or the electron velocity in *SI Appendix*, Fig. S7. In addition, when considering the energy bandwidth of free electrons, there could be an angular spread of the interfacial Cherenkov radiation in *SI Appendix*, Fig. S11.

Last but not least, the combined effect of umklapp scattering and particle–interface interactions could also enable the possibility of creating the backward Cherenkov radiation, as shown in Fig. 4 *A*–*D*. While the backward Cherenkov radiation has been extensively demonstrated from optical systems with an effective negative index or $\overline{v}_p \cdot \overline{v}_g < 0$ (66, 73–75), our revealed one from ultralow-energy electrons (e.g., with $v/c \ll 1$) that has no momentum mismatch with light in free space in Fig. 4 and *SI Appendix*, Fig. S9 has never been reported before.

While the relation between θ and v for the interfacial Cherenkov radiation could be well predicted from Eq. **1** or the result in Fig. 3*B*, the direction of its energy flow inside the photonic crystal is still elusive. To address this issue, the angular spectral energy density for the forward radiation $U_F(\theta, v)$ and the backward radiation $U_B(\theta, v)$ are separately plotted in Fig. 4 *A* and *B*, respectively. From Fig. 4 *A* and *B*, the predominant energy flow of interfacial Cherenkov radiation would propagate in opposite directions in different regimes of the electron velocity. The forward interfacial Cherenkov radiation is characterized by $U_F(\theta, v) \gg U_B(\theta, v)$ in Fig. 4*A*, and the originally excited interfacial Cherenkov radiation inside the photonic crystal propagates along the $+z$ direction in Fig. 4*C*. By contrast, the backward interfacial Cherenkov radiation begins to have $U_F(\theta, v) \ll U_B(\theta, v)$, and it propagates along the $-z$ direction inside the photonic crystal in Fig. 4*D*.

In conclusion, we have revealed that the combined effect of umklapp scattering and particle–interface interactions could provide a viable mechanism to create the interfacial Cherenkov radiation from ultralow-energy electrons that has no momentum mismatch with light in free space. This combined effect also enables a viable route to create the backward interfacial

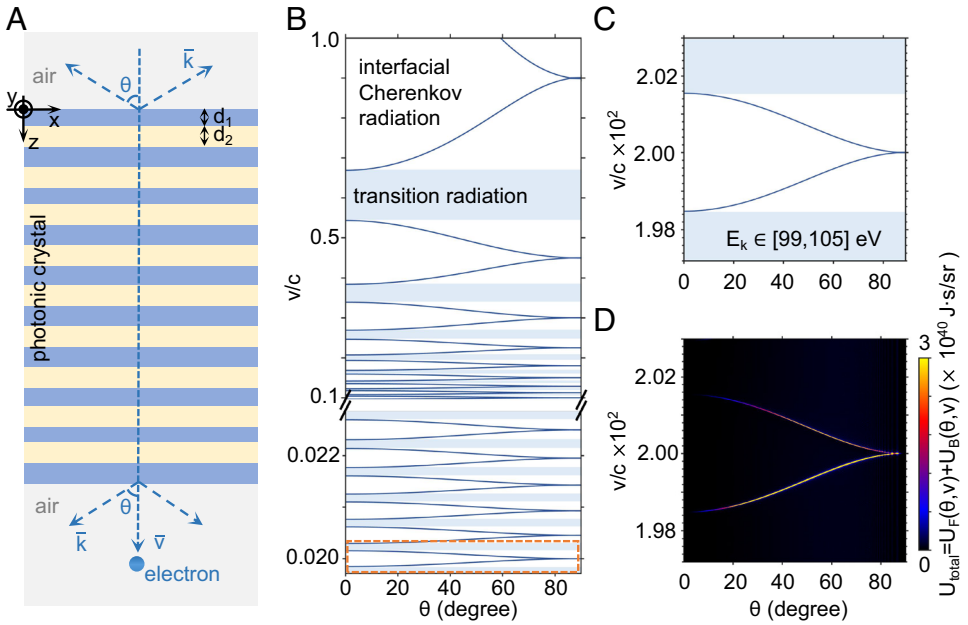

Fig. 3. Interfacial Cherenkov radiation from an ultralow-energy electron perpendicularly penetrating a photonic crystal with a finite thickness. The structural setup of the photonic crystal is the same as that in Fig. 2. (*A*) Structural schematic. The radiation θ is the angle between $\bar{v}$ ($-\bar{v}$) and $\bar{k}$ for the forward (backward) radiation. (*B* and *C*) Relation between the radiation angle of interfacial Cherenkov radiation and the electron velocity. The ultralow-velocity regime in *B* as highlighted by the orange dashed line is enlarged and replotted in *C*. (*D*) $U_{\text{total}} = U_B(\theta, v) + U_F(\theta, v)$ as a function of the electron velocity and the radiation angle, where $U_F(\theta, v)$ and $U_B(\theta, v)$ represent the angular spectral energy densities of the forward and backward radiation, respectively. The velocity range of $v/c \in [1.97, 2.03] \times 10^{-2}$ in (*C* and *D*) corresponds to the electron kinetic energy of $E_k \in [99, 105]$ eV. This velocity range is chosen to show the possibility of creating the interfacial Cherenkov radiation from low-energy electrons.

Cherenkov radiation from ultralow-energy electrons that can freely couple into free space. Moreover, we have found that the interfacial Cherenkov radiation is uniquely featured with spatially separated apexes for its wave and group cones, as intrinsically governed by the umklapp scattering for high-momentum Bloch modes. The revealed interfacial Cherenkov radiation may contribute to the development of compact on-chip light source from ultralow-energy electrons; see the discussion about integration and scalability of these light sources with enhanced photon exaction efficiency in *SI Appendix*, Figs. S12 and S13.

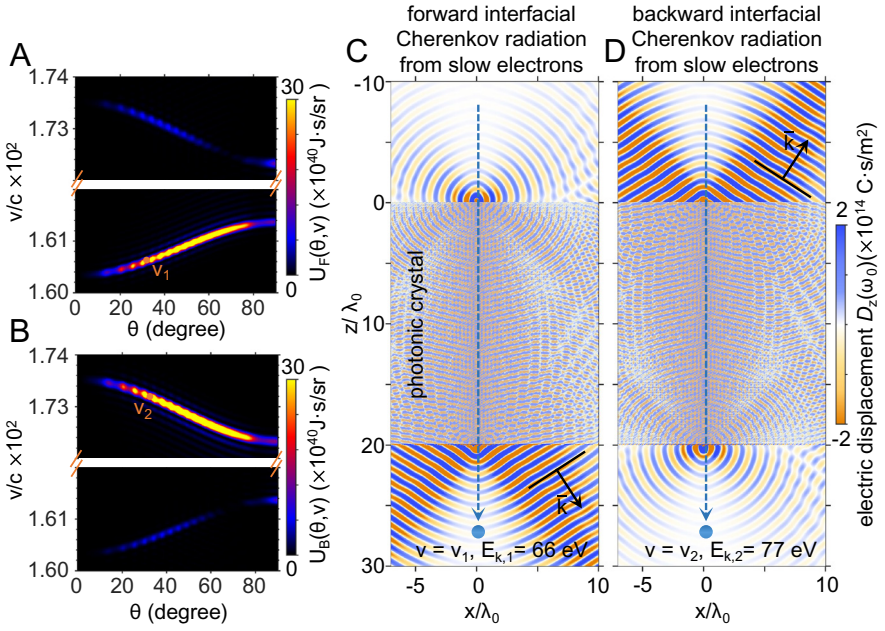

Fig. 4. Forward and backward interfacial Cherenkov radiation excited by low-energy electrons from a photonic crystal with a finite thickness. (*A*) Angular spectral energy density $U_F(\theta, v)$ of the forward free-electron radiation. (*B*) Angular spectral energy density $U_B(\theta, v)$ of the backward free-electron radiation. (*C*) Effective forward interfacial Cherenkov radiation, under the condition that the electron velocity is $v = v_1$, whose corresponding kinetic energy is $E_{k,1} = 66$ eV. (*D*) Effective backward interfacial Cherenkov radiation under the condition that the electron velocity is $v = v_2$, whose corresponding kinetic energy is $E_{k,2} = 77$ eV. These two electron velocities are chosen to demonstrate the possibility to create the forward or backward interfacial Cherenkov radiation from ultralow-energy electrons.

Materials and Methods

Deviation of Interfacial Cherenkov Radiation. Within the classical electromagnetic wave theory, we follow and extend Ginzburg and Frank's theory of transition radiation from a single interface to a multilayered system with N interfaces and $N+1$ regions, as schematically illustrated in *SI Appendix*, Fig. S1. The excited field distribution and angular spectral energy density are analytically derived in *SI Appendix*, section S1. To be specific, the field distribution in real space can be derived by performing the plane-wave expansion, that is, $\bar{E}^R(\bar{r},t)=\int d\omega d\bar{k}_\perp E^R_{\bar{k}_\perp,\omega}\, e^{i\bar{k}_\perp\bar{r}_\perp-i\omega t}$. In $\bar{k}_\perp$ and ω spaces, the distribution of radiation field in region j is obtained as

$$E^R_{\bar{k}_\perp,\omega,z,j}=\begin{cases}\dfrac{iq}{\omega\varepsilon_0(2\pi)^3}\cdot a_1\cdot e^{-ik_{z,1}(z-d_1)} & (j=1)\\ \dfrac{iq}{\omega\varepsilon_0(2\pi)^3}\left[a_j^-\cdot e^{-ik_{z,j}(z-d_j)}+a_j^+\cdot e^{ik_{z,j}(z-d_{j-1})}\right] & (2\le j\le N)\\ \dfrac{iq}{\omega\varepsilon_0(2\pi)^3}\cdot a_{N+1}\cdot e^{ik_{z,N+1}(z-d_N)} & (j=N+1)\end{cases}$$

where a_j^- (a_j^+) is the generalized factor for the backward (forward) radiation in region j, which contains the information of interference of transition radiation from multiple interfaces. Based on the knowledge of the radiation field, the backward angular spectral energy density is obtained as $U_B(\theta,v)=\frac{\varepsilon_{r,1}^{3/2}q^2\cos^2\theta|a_1|^2}{4\pi^3\varepsilon_0 c\sin^2\theta}$, and the forward angular spectral energy density is obtained as $U_F(\theta,v)=\frac{\varepsilon_{r,N+1}^{3/2}q^2\cos^2\theta|a_{N+1}|^2}{4\pi^3\varepsilon_0 c\sin^2\theta}$. Moreover, the numerical calculation of excited fields of interfacial Cherenkov radiation can be obtained with the aid of Sommerfeld integration.

More Discussion about Huygens Construction for Interfacial Cherenkov Radiation. Huygens wavelets have the shape of the ray surface and can be constructed with the knowledge of the wave-vector surface. The connection between the ray surface and the wave-vector surface is illustrated in *SI Appendix*, Fig. S2. Physical interpretation of the ray velocity and its connection with the group velocity are discussed in *SI Appendix*, section S2.

Aperture of Group Cone for the Interfacial Cherenkov Radiation. The aperture of group cone for the interfacial Cherenkov radiation is related to the group velocity $\bar{v}_g$, while the aperture of wave cone is related to the ray velocity $\bar{u}$ or the phase velocity $\bar{v}_p$. The detailed derivation is provided in *SI Appendix*, section S3 and Fig. S3.

Correspondence between Radiation Angle and Electron Velocity. We provide the detailed derivation for Eqs. **1** and **2** in *SI Appendix*, section S4.

More Discussion on the Interfacial Cherenkov Radiation. We provide more discussion on the analyses of interfacial Cherenkov radiation in *SI Appendix*, section S5. The analyses include the influence of the variation of material's permittivity and the thickness of the constituent dielectric layer on the interfacial Cherenkov radiation in *SI Appendix*, Figs. S4 and S5, the influence of material loss on the interfacial Cherenkov radiation in *SI Appendix*, Fig. S6, correlations between the order of umklapp scattering and the photon exaction efficiency in *SI Appendix*, Fig. S7, more cases of interfacial Cherenkov radiation from ultralow-energy electrons in *SI Appendix*, Figs. S8 and S9, discussion on the quantum recoil effect and radiation efficiency in *SI Appendix*, Fig. S10, influence of electron's energy bandwidth on the interfacial Cherenkov radiation in *SI Appendix*, Fig. S11, and integration and scalability of interfacial-Cherenkov-radiation-based light sources with enhanced photon exaction efficiency in *SI Appendix*, Figs. S12 and S13.

Data, Materials, and Software Availability. All theoretical and numerical findings can be reproduced based on the information in the article and/or *SI Appendix*. The data represented in all Figures is available on https://doi.org/10.5281/zenodo.8284340 (76).

ACKNOWLEDGMENTS. X.L. acknowledges the support partly from the National Natural Science Fund for Excellent Young Scientists Fund Program (Overseas) of China, the National Natural Science Foundation of China under Grant No. 62175212, Zhejiang Provincial Natural Science Fund Key Project under Grant No. LZ23F050003, and the Fundamental Research Funds for the Central Universities (2021FZZX001-19). H.C. acknowledges the support from the Key Research and Development Program of the Ministry of Science and Technology under Grants Nos. 2022YFA1404704, 2022YFA1405200, and 2022YFA1404902, the National Natural Science Foundation of China under Grants No. 61975176, the Key Research and Development Program of Zhejiang Province under Grant No. 2022C01036, and the Fundamental Research Funds for the Central Universities. J.C. acknowledges the support from the Chinese Scholarship Council (CSC No. 202206320287). B.Z. acknowledges the support from Singapore National Research Foundation Competitive Research Program No. NRF-CRP23-2019-0007. Y.Y. acknowledges the support from the start-up fund of the University of Hong Kong and the National Natural Science Foundation of China Excellent Young Scientists Fund (HKU 12222417).

Author affiliations: [a]Interdisciplinary Center for Quantum Information, State Key Laboratory of Extreme Photonics and Instrumentation, ZJU-Hangzhou Global Scientific and Technological Innovation Center, Zhejiang University, Hangzhou 310027, China; [b]International Joint Innovation Center, The Electromagnetics Academy at Zhejiang University, Zhejiang University, Haining 314400, China; [c]Department of Electrical and Computer Engineering, Technion-Israel Institute of Technology, Haifa 32000, Israel; [d]School of Physics, Zhejiang University, Hangzhou 310027, China; [e]Key Laboratory of Advanced Micro/Nano Electronic Devices & Smart Systems of Zhejiang, Jinhua Institute of Zhejiang University, Zhejiang University, Jinhua 321099, China; [f]College of Electronic and Information Engineering, Nanjing University of Aeronautics and Astronautics, Nanjing 211106, China; [g]Department of Physics, University of Hong Kong, Hong Kong 999077, China; [h]Division of Physics and Applied Physics, School of Physical and Mathematical Sciences, Nanyang Technological University, Singapore 637371, Singapore; [i]Centre for Disruptive Photonic Technologies, Nanyang Technological University, Singapore 637371, Singapore; and [j]Shaoxing Institute of Zhejiang University, Zhejiang University, Shaoxing 312000, China

1. P. A. Cherenkov, Visible emission of clean liquids by action of gamma radiation. *Dokl. Akad. Nauk SSSR* **2**, 451–454 (1934).
2. C. Roques-Carmes *et al.*, Free-electron-light interactions in nanophotonics. *Appl. Phys. Rev.* **10**, 011303 (2023).
3. Y. Adiv *et al.*, Observation of 2D Cherenkov radiation. *Phys. Rev. X* **13**, 011002 (2023).
4. Y. Yang *et al.*, Photonic flatband resonances for free-electron radiation. *Nature* **613**, 42–47 (2023).
5. A. Dikopoltsev *et al.*, Light emission by free electrons in photonic time-crystals. *Proc. Natl. Acad. Sci. U.S.A.* **119**, e2119705119 (2022).
6. H. Hu *et al.*, Surface Dyakonov–Cherenkov radiation. *eLight* **2**, 2 (2022).
7. P. Genevet *et al.*, Controlled steering of Cherenkov surface plasmon wakes with a one-dimensional metamaterial. *Nat. Nanotechnol.* **10**, 804–809 (2015).
8. O. Chamberlain, E. Segrè, C. Wiegand, T. Ypsilantis, Observation of antiprotons. *Phys. Rev.* **100**, 947–950 (1955).
9. J. J. Aubert *et al.*, Experimental observation of a heavy particle. *J. Phys. Rev. Lett.* **33**, 1404–1406 (1974).
10. M. Amenomori *et al.*, First detection of sub-PeV diffuse gamma rays from the galactic disk: Evidence for ubiquitous galactic cosmic rays beyond PeV energies. *Phys. Rev. Lett.* **126**, 141101 (2021).
11. X. Lin *et al.*, A Brewster route to Cherenkov detectors. *Nat. Commun.* **12**, 5554 (2021).
12. M. Adinolfi *et al.*, Performance of the LHCb RICH detector at the LHC. *Eur. Phys. J. C* **73**, 2431 (2013).
13. X. Lin *et al.*, Controlling Cherenkov angles with resonance transition radiation. *Nat. Phys.* **14**, 816–821 (2018).
14. G. Adamo *et al.*, Light well: A tunable free-electron light source on a chip. *Phys. Rev. Lett.* **103**, 113901 (2009).
15. S. Liu *et al.*, Surface polariton Cherenkov light radiation source. *Phys. Rev. Lett.* **109**, 153902 (2012).
16. F. Liu *et al.*, Integrated Cherenkov radiation emitter eliminating the electron velocity threshold. *Nat. Photon.* **11**, 289–292 (2017).
17. R. L. Hachadorian *et al.*, Imaging radiation dose in breast radiotherapy by X-ray CT calibration of Cherenkov light. *Nat. Commun.* **11**, 2298 (2020).
18. D. A. Alexander *et al.*, Color Cherenkov imaging of clinical radiation therapy. *Light Sci. Appl.* **10**, 226 (2021).
19. T. M. Shaffer, E. C. Pratt, J. Grimm, Utilizing the power of Cerenkov light with nanotechnology. *Nat. Nanotechnol.* **12**, 106–117 (2017).
20. X. Wang *et al.*, Cherenkov luminescence in tumor diagnosis and treatment: A review. *Photonics* **9**, 390 (2022).
21. N. Kotagiri, G. P. Sudlow, W. J. Akers, S. Achilefu, Breaking the depth dependency of phototherapy with Cerenkov radiation and low-radiance-responsive nanophotosensitizers. *Nat. Nanotechnol.* **10**, 370–379 (2015).
22. A. Kamkaew *et al.*, Cerenkov radiation induced photodynamic therapy using chlorin e6-loaded hollow mesoporous silica nanoparticles. *ACS Appl. Mater. Interfaces* **8**, 26630–26637 (2016).
23. I. E. Tamm, I. M. Frank, Coherent radiation of fast electrons in a medium. *Dokl. Akad. Nauk SSSR* **14**, 107–112 (1937).
24. I. Tamm, Radiation emitted by uniformly moving electrons. *J. Phys. (USSR)* **1**, 439–454 (1939).

25. I. Kaminer *et al.*, Efficient plasmonic emission by the quantum Čerenkov effect from hot carriers in graphene. *Nat. Commun.* **7**, 11880 (2016).
26. A. Massuda *et al.*, Smith–Purcell radiation from low-energy electrons. *ACS Photonics* **5**, 3513–3518 (2018).
27. Y.Y. Auad *et al.*, μeV electron spectromicroscopy using free-space light. *Nat. Commun.* **14**, 4442 (2023).
28. N. Talebi, Strong interaction of slow electrons with near-field light visited from first principles. *Phys. Rev. Lett.* **125**, 080401 (2020).
29. M. Eldar, Y. Pan, M. Krüger, Self-trapping of slow electrons in the energy domain. arXiv [Preprint] (2022). https://doi.org/10.48550/arXiv.2209.14850 (Accessed 10 April 2023).
30. Y. Hochberg *et al.*, Determining dark-matter–electron scattering rates from the dielectric function. *Phys. Rev. Lett.* **127**, 151802 (2021).
31. T. Zhang *et al.*, Tunable optical topological transition of Cherenkov radiation. *Photonics Res.* **10**, 1650–1660 (2022).
32. H. Hu *et al.*, Nonlocality induced Cherenkov threshold. *Laser Photon. Rev.* **14**, 2000149 (2020).
33. A. A. Orlov, P. M. Voroshilov, P. A. Belov, Y. S. Kivshar, Engineered optical nonlocality in nanostructured metamaterials. *Phys. Rev. B* **84**, 045424 (2011).
34. W. Yan, M. Wubs, N. A. Mortensen, Hyperbolic metamaterials: Nonlocal response regularizes broadband supersingularity. *Phys. Rev. B* **86**, 205429 (2012).
35. L. Shen *et al.*, Broadband enhancement of on-chip single-photon extraction via tilted hyperbolic metamaterials. *Appl. Phys. Rev.* **7**, 021403 (2020).
36. D. Lu, J. J. Kan, E. E. Fullerton, Z. Liu, Enhancing spontaneous emission rates of molecules using nanopatterned multilayer hyperbolic metamaterials. *Nat. Nanotechnol.* **9**, 48–53 (2014).
37. T. Galfsky, J. Gu, E. E. Narimanov, V. M. Menon, Photonic hypercrystals for control of light–matter interactions. *Proc. Natl. Acad. Sci. U.S.A.* **114**, 5125–5129 (2017).
38. T. Galfsky *et al.*, Active hyperbolic metamaterials: Enhanced spontaneous emission and light extraction. *Optica* **2**, 62–65 (2015).
39. A. Poddubny, I. Iorsh, P. Belov, Y. Kivshar, Hyperbolic metamaterials. *Nat. Photon.* **7**, 948–957 (2013).
40. D. Lee *et al.*, Hyperbolic metamaterials: Fusing artificial structures to natural 2D materials. *eLight* **2**, 1 (2022).
41. N. v Sapra, *et al.*, On-chip integrated laser-driven particle accelerator. *Science* **367**, 79–83 (2020).
42. Y. Yang *et al.*, Maximal spontaneous photon emission and energy loss from free electrons. *Nat. Phys.* **14**, 894–899 (2018).
43. L. J. Wong, I. Kaminer, O. Ilic, J. D. Joannopoulos, M. Soljačić, Towards graphene plasmon-based free-electron infrared to X-ray sources. *Nat. Photon.* **10**, 46–52 (2016).
44. A. Polman, M. Kociak, F. J. G. de Abajo, Electron–beam spectroscopy for nanophotonics. *Nat. Mater.* **18**, 1158–1171 (2019).
45. M. Henstridge *et al.*, Synchrotron radiation from an accelerating light pulse. *Science* **362**, 439–442 (2018).
46. A. Feist *et al.*, Cavity-mediated electron-photon pairs. *Science* **377**, 777–780 (2022).
47. D. Zhang *et al.*, Coherent surface plasmon polariton amplification via free-electron pumping. *Nature* **611**, 55–60 (2022).
48. S. Huang *et al.*, Quantum recoil in free-electron interactions with atomic lattices. *Nat. Photon.* **17**, 224–230 (2023).
49. S. Tsesses *et al.*, Tunable photon-induced spatial modulation of free electrons. *Nat. Mater.* **22**, 345–352 (2023).
50. H. Hu, X. Lin, Y. Luo, Free-electron radiation engineering via structured environments. *Prog. Electromagn. Res.* **171**, 75–88 (2021).
51. V. L. Ginzburg, I. M. Frank, Radiation of a uniformly moving electron due to its transition from one medium into another. *J. Phys. (USSR)* **9**, 353–362 (1945).
52. V. L. Ginzburg, *Transition Radiation and Transition Scattering* (A. Hilger, 1990).
53. I. P. Ivanov, D. V. Karlovets, Detecting transition radiation from a magnetic moment. *Phys. Rev. Lett.* **110**, 264801 (2013).
54. R. Chen *et al.*, Recent advances of transition radiation: Fundamentals and applications. *Mater. Today Electron.* **3**, 100025 (2023).
55. C. Luo, M. Ibanescu, S. G. Johnson, J. D. Joannopoulos, Cerenkov radiation in photonic crystals. *Science* **299**, 368–371 (2003).
56. F. J. G. de Abajo, Optical excitations in electron microscopy. *Rev. Mod. Phys.* **82**, 209 (2010).
57. C. Kremers, D. N. Chigrin, J. Kroha, Theory of Cherenkov radiation in periodic dielectric media: Emission spectrum. *Phys. Rev. A* **79**, 013829 (2009).
58. C. Kremers, D. N. Chigrin, Spatial distribution of Cherenkov radiation in periodic dielectric media. *J. Opt. A* **11**, 114008 (2009).
59. F. J. G. de Abajo *et al.*, Cherenkov effect as a probe of photonic nanostructures. *Phys. Rev. Lett.* **91**, 143902 (2003).
60. A. Sommerfeld, *Optics* (Academic Press, 1954).
61. M. Born, E. Wolf, *Principles of Optics: Electromagnetic Theory of Propagation, Interference and Diffraction of Light* (Cambridge University Press, 1999).
62. I. M. Frank, On some peculiarities of Vavilov–Cherenkov radiation. *Nucl. Instrum. Methods Phys. Res. A* **248**, 7–12 (1986).
63. L. Brillouin, *Wave Propagation and Group Velocity* (Academic Press, 1960).
64. J. A. Stratton, *Electromagnetic Theory* (McGraw-Hill, 1941).
65. L. D. Landau, E. M. Lifshitz, *Electrodynamics of Continuous Media* (Pergamon, 1984).
66. H. Chen, M. Chen, Flipping photons backward: Reversed Cherenkov radiation. *Mater. Today* **14**, 34–41 (2011).
67. I. Carusotto, M. Artoni, G. C. la Rocca, F. Bassani, Slow group velocity and Cherenkov radiation. *Phys. Rev. Lett.* **87**, 064801 (2001).
68. X. Lin *et al.*, Splashing transients of 2D plasmons launched by swift electrons. *Sci. Adv.* **3**, e1601192 (2017).
69. J. Chen, H. Chen, X. Lin, Photonic and plasmonic transition radiation from graphene. *J. Opt.* **23**, 034001 (2021).
70. J. Chen *et al.*, Low-velocity-favored transition radiation. arXiv [Preprint] (2022). https://doi.org/10.48550/arXiv.2212.13066 (Accessed 2 January 2023).
71. F. Tay *et al.*, Bulk-Plasmon-Mediated Free-Electron Radiation Beyond the Conventional Formation Time. Advanced Science **10**, 2300760 (2023).
72. R. Chen *et al.*, Free-electron Brewster-transition radiation. *Sci. Adv.* **9**, eadh8098 (2023).
73. S. Xi *et al.*, Experimental verification of reversed Cherenkov radiation in left-handed metamaterial. *Phys. Rev. Lett.* **103**, 194801 (2009).
74. Z. Duan *et al.*, Observation of the reversed Cherenkov radiation. *Nat. Commun.* **8**, 14901 (2017).
75. V. G. Veselago, Electrodynamics of substances with simultaneously negative ε and μ. *Sov. Phys. Usp.* **10**, 509–514 (1968).
76. Z. Gong, Interfacial Cherenkov radiation from ultralow-energy electrons – Data set [Data set]. Zenodo. https://doi.org/10.5281/zenodo.8284340. Deposited 26 August 2023.

Supplementary Information for

"Interfacial Cherenkov radiation from ultralow-energy electrons"

Supplementary Information Guide:

Section S1: Derivation of interfacial Cherenkov radiation

In this section, we analytically derive the field distribution and angular spectral energy density of interfacial Cherenkov radiation by following and extending Ginzburg and Frank's theory of transition radiation from single interface [51,52].

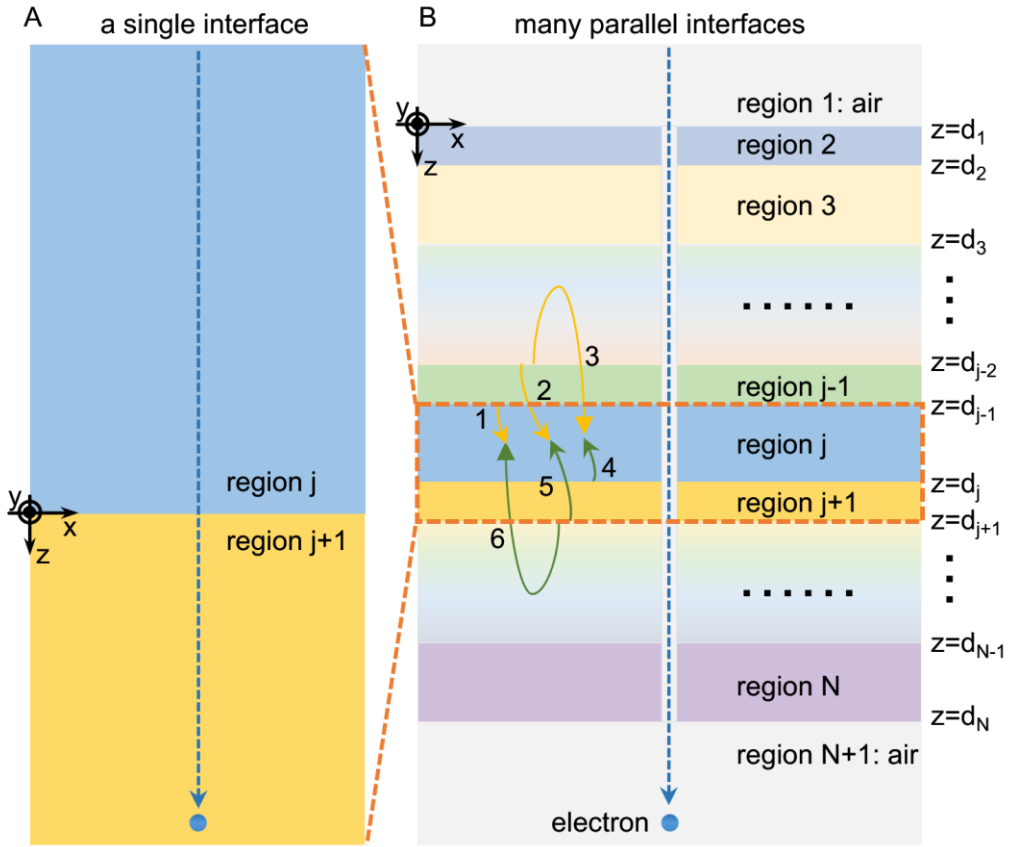

Fig. S1. Structural schematic of light emission from particle-interface interactions. (*A*) Transition radiation from a single interface. (*B*) Interference of transition radiation from multiple parallel interfaces.

S1.1 Transition radiation from a single interface

In this subsection, we provide the detailed derivation of transition radiation from a single interface in Fig. S1*A*. An electron with a charge q and a velocity $\bar{v} = \hat{z}v$ perpendicularly penetrates an interface between region j and region $j+1$, i.e., the interface lying at the plane of $z = d_j$. The dielectric region j has a relative permittivity $\varepsilon_{r,j}$. The induced current density is $\bar{J}(\bar{r},t) = qv\delta(x)\delta(y)\delta(z-vt)$. By performing the plane-wave expansion to the source and all fields, we have

$$\bar{J}(\bar{r},t)=\int d\omega\ d\bar{k}_{\perp}(z)\bar{J}_{\bar{k}_{\perp},\omega}e^{i\bar{k}_{\perp}\bar{r}_{\perp}-i\omega t}$$
$$\bar{H}(\bar{r},t)=\int d\omega\, d\bar{k}_{\perp}\bar{H}_{\bar{k}_{\perp},\omega}(z)e^{i\bar{k}_{\perp}\bar{r}_{\perp}-i\omega t} \tag{S1}$$
$$\bar{E}(\bar{r},t)=\int d\omega\, d\bar{k}_{\perp}\bar{E}_{\bar{k}_{\perp},\omega}(z)e^{i\bar{k}_{\perp}\bar{r}_{\perp}-i\omega t}$$

where the excited field has a wavevector of $\bar{k}=\hat{\perp}\,k_{\perp}+\hat{z}k_z$, and the subscript $\perp$ indicates the component of the wavevector perpendicular to the electron trajectory. From equation (S1), one has $\bar{J}_{\bar{k}_{\perp},\omega}=\hat{z}\frac{q}{(2\pi)^3}e^{i\frac{\omega}{v}z}$. For the simplicity of expression, the subscripts $\bar{k}_{\perp}$ and ω are ignored in the following.

By solving Maxwell's equations, in a medium with permittivity ε and permeability μ, we have the equations that govern H_z and E_z, namely

$$\left(\frac{\partial^2}{\partial z^2}+\omega^2\mu\varepsilon+\nabla_{\perp}^2\right)\begin{pmatrix}E_z\\H_z\end{pmatrix}=\begin{pmatrix}-\left(\frac{\partial^2}{\partial z^2}+\omega^2\mu\varepsilon\right)\frac{J_z}{i\omega\varepsilon}-\nabla_{\perp}\cdot\frac{\partial\bar{J}_{\perp}}{\partial z}\\-\frac{\nabla_{\perp}\cdot\frac{\partial}{\partial z}\bar{J}_{\perp}}{i\omega\mu}\end{pmatrix} \tag{S2}$$

where $\bar{J}=\bar{J}_{\perp}+\hat{z}J_z$. Because $\bar{J}_{\perp}=0$, we have $H_z=0$. This way, all excited fields are transverse-magnetic (TM, or *p*-polarized) waves. Substituting J_z into equation (S2), we have

$$E_z=E_z^q+E_z^R$$
$$E_{z,j}^q=-\frac{iq}{\omega\varepsilon_0(2\pi)^3}\frac{1-\frac{c^2}{v^2\varepsilon_{\mathrm{r},j}}}{\varepsilon_{\mathrm{r}.j}-\frac{c^2}{v^2}-\frac{k_{\perp}^2c^2}{\omega^2}}e^{\frac{i\omega}{v}z}$$
$$E_{z,j+1}^q=-\frac{iq}{\omega\varepsilon_0(2\pi)^3}\frac{1-\frac{c^2}{v^2\varepsilon_{\mathrm{r},j+1}}}{\varepsilon_{\mathrm{r}.j+1}-\frac{c^2}{v^2}-\frac{k_{\perp}^2c^2}{\omega^2}}e^{\frac{i\omega}{v}z} \tag{S3}$$
$$E_{z,j}^R=\frac{iq}{\omega\varepsilon_0(2\pi)^3}a_{j|j+1}^{-}e^{-k_{z,j}(z-d_j)}$$
$$E_{z,j+1}^R=\frac{iq}{\omega\varepsilon_0(2\pi)^3}a_{j|j+1}^{+}e^{k_{z,j+1}(z-d_j)}$$

where c is the speed of light in free space, ε_0 is the permittivity of free space, E^q is the charge field, E^R stands for the radiation field, and the component of wavevector along z direction in region j is $k_{z,j}=\sqrt{\frac{\omega^2}{c^2}\varepsilon_{\mathrm{r},j}-k_{\perp}^2}$. Moreover, $a_{j|j+1}^{-}$ ($a_{j|j+1}^{+}$) is the factor of the backward (forward) radiation from the $j|j+1$ interface at the plane of $z=d_j$. They can be expressed as

$$a_{j|j+1}^{-}=a_{j|j+1}^{-,0}e^{\frac{i\omega}{v}d_j}$$
$$a_{j|j+1}^{+}=a_{j|j+1}^{+,0}e^{\frac{i\omega}{v}d_j} \tag{S4}$$

where $a_{j|j+1}^{-,0}$ ($a_{j|j+1}^{+,0}$) is the factor of the backward (forward) radiation from the $j|j+1$ interface, if $d_j = 0$. By matching the boundary conditions at $z = 0$, one further has

$$a_{j|j+1}^{-,0} = \frac{\frac{v}{c}\frac{k_\perp^2 c^2}{\omega^2 \varepsilon_{\mathrm{r},j}}\left(\varepsilon_{\mathrm{r},j+1}-\varepsilon_{\mathrm{r},j}\right)\left(1-\frac{v^2}{c^2}\varepsilon_{\mathrm{r},j}+\frac{v}{c}\frac{k_{z,j+1}}{\omega/c}\right)}{\left(1-\frac{v^2}{c^2}\varepsilon_{\mathrm{r},j}+\frac{k_\perp^2 v^2}{\omega^2}\right)\left(1+\frac{v}{c}\frac{k_{z,j+1}}{\omega/c}\right)\left(\varepsilon_{\mathrm{r},j}\frac{k_{z,j+1}}{\omega/c}+\varepsilon_{\mathrm{r},j+1}\frac{k_{z,j}}{\omega/c}\right)}$$
$$a_{j|j+1}^{+,0} = \frac{\frac{v}{c}\frac{k_\perp^2 c^2}{\omega^2 \varepsilon_{\mathrm{r},j+1}}\left(\varepsilon_{\mathrm{r},j+1}-\varepsilon_{\mathrm{r},j}\right)\left(1-\frac{v^2}{c^2}\varepsilon_{\mathrm{r},j+1}-\frac{v}{c}\frac{k_{z,j}}{\omega/c}\right)}{\left(1-\frac{v^2}{c^2}\varepsilon_{\mathrm{r},j+1}+\frac{k_\perp^2 v^2}{\omega^2}\right)\left(1-\frac{v}{c}\frac{k_{z,j}}{\omega/c}\right)\left(\varepsilon_{\mathrm{r},j}\frac{k_{z,j+1}}{\omega/c}+\varepsilon_{\mathrm{r},j+1}\frac{k_{z,j}}{\omega/c}\right)} \quad \text{(S5)}$$

After some calculations based on equations (S1-S5), one can express all fields in the cylindrical coordinates (ρ, ϕ, z), namely

$$\bar{E}_z(\bar{r},t) = \bar{E}_z^q(\bar{r},t) + \bar{E}_z^R(\bar{r},t)$$
$$\bar{E}_{z,j}^q(\bar{r},t) = \hat{z}\int_{-\infty}^{\infty} d\omega \frac{-q}{8\pi\omega\varepsilon_0\varepsilon_{\mathrm{r},j}}\left(\frac{\omega^2}{c^2}\varepsilon_{\mathrm{r},j}-\frac{\omega^2}{v^2}\right)H_0^{(1)}\left(\rho\sqrt{\frac{\omega^2}{c^2}\varepsilon_{\mathrm{r},j}-\frac{\omega^2}{v^2}}\right)e^{i\frac{\omega}{v}z-\omega t}$$
$$\bar{E}_{z,j}^R(\bar{r},t) = \hat{z}\int_{-\infty}^{\infty} d\omega \int_0^{\infty} dk_\perp \frac{iq}{\omega\varepsilon_0(2\pi)^3}a_{j|j+1}^{-}\left(2\pi k_\perp J_0(k_\perp\rho)\right)e^{-ik_{z,j}(z-d_j)-i\omega t} \quad \text{(S6)}$$
$$\bar{E}_{z,j+1}^q(\bar{r},t) = \hat{z}\int_{-\infty}^{\infty} d\omega \frac{-q}{8\pi\omega\varepsilon_0\varepsilon_{\mathrm{r},j+1}}\left(\frac{\omega^2}{c^2}\varepsilon_{\mathrm{r},j+1}-\frac{\omega^2}{v^2}\right)H_0^{(1)}\left(\rho\sqrt{\frac{\omega^2}{c^2}\varepsilon_{\mathrm{r},j+1}-\frac{\omega^2}{v^2}}\right)e^{i\frac{\omega}{v}z-\omega t}$$
$$\bar{E}_{z,j+1}^R(\bar{r},t) = \hat{z}\int_{-\infty}^{\infty} d\omega \int_0^{\infty} dk_\perp \frac{iq}{\omega\varepsilon_0(2\pi)^3}a_{j|j+1}^{+}\left(2\pi k_\perp J_0(k_\perp\rho)\right)e^{ik_{z,j+1}(z-d_j)-i\omega t}$$

where $H_0^{(1)}$ and $H_1^{(1)}$ represent the first kind of Hankel function of zero order and first order, respectively; J_0 is the first kind of Bessel function of zero order. From equations (S2,S6), the field components perpendicular to the particle trajectory, namely $\bar{H}_\perp$ and $\bar{E}_\perp$, can be expressed as

$$\bar{E}_\perp = \frac{i\omega\mu(\nabla_\perp \times \bar{H}_z - \bar{J}_\perp) + \nabla_\perp \frac{\partial E_z}{\partial z}}{\frac{\partial^2}{\partial z^2} + \omega^2\mu\varepsilon}$$
$$\bar{H}_\perp = \frac{-i\omega\varepsilon\nabla_\perp \times \bar{E}_z - \hat{z}\times\frac{\partial \bar{J}_\perp}{\partial z} + \nabla_\perp \frac{\partial H_z}{\partial z}}{\frac{\partial^2}{\partial z^2} + \omega^2\mu\varepsilon} \quad \text{(S7)}$$

S1.2 Interference of transition radiation from multiple parallel interfaces

In this subsection, we calculate the interference of transition radiation from multiple parallel interfaces ($j|j+1$ interface, $\forall j = 1,2,\ldots N$), as illustrated in Fig. S1*B*, the total electromagnetic field in region *j* originates from the interfaces above the region *j* and those below it. We first calculate the field in region *j* originating from the light emission from the interfaces above the region *j* which can be further divided into parts 1, 2 and 3.

Part 1: Field in region j from the forward transition radiation at the $j-1|j$ interface

From the viewpoint of geometric optics, the forward transition radiation at the $j-1|j$ interface contributing to the field in region j is

$$\begin{aligned} TR_j^+ \to Region\ j\ &= A_{j,0}^+ \cdot \left[e^{ik_{z,j}(z-d_{j-1})} + \tilde{R}_{j|j+1} e^{2ik_{z,j}(d_j-d_{j-1})} e^{-ik_{z,j}(z-d_{j-1})}\right] \\ A_{j,0}^+ &= \frac{iq}{\omega\varepsilon_0(2\pi)^3} \cdot a_{j-1|j}^+ \cdot M_j \\ M_j &= \frac{1}{1-\tilde{R}_{j|j+1}\tilde{R}_{j|j-1}e^{2ik_{z,j}(d_j-d_{j-1})}} \end{aligned} \tag{S8}$$

where $a_{j-1|j}^+$ is the radiation factor of the forward transition radiation at the $j-1|j$ interface determined by equation (S4); M_j characterizes the multiple reflections at the $j-1|j$ and $j|j+1$ interfaces, and we have $M_1 = M_{N+1} = 1$; $\tilde{R}_{j|j-1}$ and $\tilde{R}_{j|j+1}$ are the generalized reflection and transmission coefficients for TM waves at the $j-1|j$ and $j|j+1$ interfaces, respectively. The subscript of $\tilde{R}_{j|j+1}$ and $\tilde{R}_{j|j-1}$ indicates that the TM plane wave is incident from region j (the first number) and transmitted to region $j+1$ or $j-1$ (the second number), respectively. This rule applies for other reflection and transmission coefficients of TM waves in the following. $\tilde{R}_{j|j+1}$ and $\tilde{R}_{j|j-1}$ can be obtained by using an iteration relationship [76], namely

$$\begin{aligned} \tilde{R}_{j|j+1} &= R_{j|j+1} + \frac{T_{j|j+1}\tilde{R}_{j+1|j+2}T_{j+1|j}e^{2ik_{z,j+1}(d_{j+1}-d_j)}}{1-R_{j+1|j}\tilde{R}_{j+1|j+2}e^{2ik_{z,j+1}(d_{j+1}-d_j)}} \\ \tilde{R}_{j|j-1} &= R_{j|j-1} + \frac{T_{j|j-1}\tilde{R}_{j-1|j-2}T_{j-1|j}e^{2ik_{z,j-1}(d_{j-1}-d_{j-2})}}{1-R_{j-1|j}\tilde{R}_{j-1|j-2}e^{2ik_{z,j-1}(d_{j-1}-d_{j-2})}} \end{aligned} \tag{S9}$$

The iteration in equation (S9) can start from the first or the last interface due to the facts that $\tilde{R}_{N|N+1} = R_{N|N+1}$ and $\tilde{R}_{2|1} = R_{2|1}$. The reflection and transmission coefficient for the field E_z at interface $z = d_j$ from region j to region $j+1$ can be expressed as $T_{j|j+1} = T^{\mathrm{TM}}\frac{\varepsilon_{\mathrm{r},j}}{\varepsilon_{\mathrm{r},j+1}} = \frac{2\varepsilon_{\mathrm{r},j+1}k_{z,j}}{\varepsilon_{\mathrm{r},j+1}k_{z,j}+\varepsilon_{\mathrm{r},j}k_{z,j+1}} \cdot \frac{\varepsilon_{\mathrm{r},j}}{\varepsilon_{\mathrm{r},j+1}}$ and $R_{j|j+1} = R^{\mathrm{TM}} = \frac{\varepsilon_{\mathrm{r},j+1}k_{z,j}-\varepsilon_{\mathrm{r},j}k_{z,j+1}}{\varepsilon_{\mathrm{r},j+1}k_{z,j}+\varepsilon_{\mathrm{r},j}k_{z,j+1}}$, where $R^{\mathrm{TM}}, T^{\mathrm{TM}}$ are the reflection and transmission coefficients defined for the magnetic field $H_\perp$. Similarly, from region j to region $j+1$, we have $T_{j+1|j} = \frac{2\varepsilon_{\mathrm{r},j}k_{z,j+1}}{\varepsilon_{\mathrm{r},j+1}k_{z,j}+\varepsilon_{\mathrm{r},j}k_{z,j+1}} \cdot \frac{\varepsilon_{\mathrm{r},j+1}}{\varepsilon_{\mathrm{r},j}}$ and $R_{j+1|j} = -R_{j|j+1} = -\frac{\varepsilon_{\mathrm{r},j+1}k_{z,j}-\varepsilon_{\mathrm{r},j}k_{z,j+1}}{\varepsilon_{\mathrm{r},j+1}k_{z,j}+\varepsilon_{\mathrm{r},j}k_{z,j+1}}$.

Part 2: Field in region j from the forward transition radiation at the $m-1|m$ $(2 \le m \le j-1)$ interface

Only part of the forward transition radiation at the $m-1|m$ $(2 \le m \le j-1)$ interface would transmit into region j $(j > m)$. These transmitted fields in region j can be expressed as

$$TR_m^+ \to Region\ j = C_{m|j}^+\left[e^{ik_{z,j}(z-d_{m-1})} + \tilde{R}_{j|j+1}e^{2ik_{z,j}(d_j-d_{m-1})}e^{-ik_{z,j}(z-d_{m-1})}\right] \quad \text{(S10)}$$

The only unknown quantity $C_{m|j}^+$ can be obtained by recursively matching boundary conditions from region m to region j. For example, at the $z = d_m$ interface, we have

$$C_{m|m+1}^+ e^{ik_{z,m+1}(d_m-d_{m-1})} = A_{m,0}^+ e^{ik_{z,m}(d_m-d_{m-1})} \cdot S_{m|m+1} \quad \text{(S11)}$$

$$S_{m|m+1} = \frac{T_{m|m+1}}{1 - R_{m+1|m}\tilde{R}_{m+1|m+2}e^{i2k_{z,m+1}(d_{m+1}-d_m)}} \quad \text{(S12)}$$

Namely, the value of $C_{m|m+1}^+$ is determined by $A_{m,0}^+$ and the transmission at the $m|m+1$ interface. Following equation (S12), we have

$$\prod_{n=m}^{n=j-1} C_{m|n+1}^+ e^{ik_{z,n+1}(d_n-d_{m-1})} = \prod_{n=m}^{n=j-1} C_{m|n}^+ e^{ik_{z,n}(d_n-d_{m-1})} \cdot S_{n|n+1} \quad \text{(S13)}$$

Especially, $C_{m|m}^+ = A_{m,0}^+$. From equation (S13), one has

$$C_{m|j}^+ e^{ik_{z,j}(d_{j-1}-d_{m-1})} = \tilde{T}_{m|j}^{j>m} \cdot A_{m,0}^+ \quad \text{(S14)}$$

$$\tilde{T}_{m|j}^{j>m} = \prod_{n=m}^{n=j-1} S_{n|n+1}\, e^{ik_{z,n}(d_n-d_{n-1})} \quad \text{(S15)}$$

where $\tilde{T}_{m|j}^{j>m}$ can be treated as the generalized transmission coefficient from region m to region j.

Part 3: Field in region j from the forward transition radiation at the $m|m+1$ $(2 \le m \le j-1)$ interface

The emitted field in region m from the backward transition radiation at the $m|m+1$ interface is written as

$$\begin{gathered} TR_m^- \to Region\ m = A_{m,o}^-\left[e^{-ik_{z,m}(z-d_m)} + \tilde{R}_{m|m-1}e^{ik_{z,m}(z-d_m)} \cdot e^{-2ik_{z,m}(d_{m-1}-d_m)}\right] \\ A_{m,o}^- = \frac{iq}{\omega\varepsilon_0(2\pi)^3} \cdot a_{m|m+1}^- \cdot M_m \end{gathered} \quad \text{(S16)}$$

where the backward radiation factor $a_{m|m+1}^-$ of $m|m+1$ interface can be obtained from equation (S4). Equivalently, the emitted field in region m can be transformed to

$$\begin{gathered} TR_m^- \to Region\ m = B_{m,o}^- e^{-ik_{z,m}(z-d_m)} + BR_{m,o}^+\left[e^{+ik_{z,m}(z-d_m)} + \tilde{R}_{m|m+1}e^{-ik_{z,m}(z-d_m)}e^{+2ik_{z,m}(d_m-d_m)}\right] \\ BR_{m,o}^+ = B_{m,o}^- M_m \tilde{R}_{m|m-1}e^{-2ik_{z,m}(d_{m-1}-d_m)} \\ B_{m,o}^- = \frac{A_{m,o}^-}{M_m} = \frac{iq}{\omega\varepsilon_0(2\pi)^3} \cdot a_{m|m+1}^- \end{gathered} \quad \text{(S17)}$$

In the transformation above, the relation of $M_m = 1 + M_m\tilde{R}_{m|m+1}\tilde{R}_{m|m-1}e^{2ik_{z,m}(d_m-d_{m-1})}$ is used. When calculating the field distribution in transmitted region j $(j > m)$ from the backward transition radiation at the $m|m+1$ interface, we only need to consider the part relevant to $BR_{m,o}^+$ in equation (S17).

Similar to equation (S11), we can express the transmitted field into region j as

$$TR_m^- \to Region\ j = D_{m|j}^+\left[e^{ik_{z,j}(z-d_m)} + \tilde{R}_{j|j+1}e^{2ik_{z,j}(d_j-d_m)}e^{-ik_{z,j}(z-d_m)}\right] \tag{S18}$$

The calculation procedure for the unknown factor $D_{m|j}^+$ is the same as that of $C_{m|j}^+$. After some algebra, we have

$$D_{m|j}^+ e^{ik_{z,j}(d_{j-1}-d_m)} = \tilde{T}_{m|j}^{j>m} BR_{m,o}^+ \cdot e^{ik_{z,m}(d_{m-1}-d_m)} \tag{S19}$$

where $\tilde{T}_{m|j}^{j>m}$ is determined by equation (S15).

Below, we proceed to derive the field in region j from the transition radiation at the interfaces below region j.

Part 4: Field in region j from the backward transition radiation at the $j|j+1$ interface

We first calculate the field in region j from the backward transition radiation at the $j|j+1$ interface. This part of radiation has actually been tackled in equation (S16). Namely, the related field is written as

$$\begin{gathered} TR_j^- \to region\ j = A_{j,o}^-\left[e^{-ik_{z,j}(z-d_j)} + \tilde{R}_{j|j-1}e^{+ik_{z,j}(z-d_j)} \cdot e^{-2ik_{z,j}(d_{j-1}-d_j)}\right] \\ A_{j,o}^- = \frac{iq}{\omega\varepsilon_0(2\pi)^3} \cdot a_{j|j+1}^{-,o} e^{i\frac{\omega}{v}d_j} \cdot M_j \end{gathered} \tag{S20}$$

Part 5: Field in region j from the backward transition radiation at the $m|m+1$ $(j+1 \le m \le N)$ interface

The field in region j $(j < m)$ can be expressed as

$$TR_m^- \to region\ j = D_{m|j}^-\left[e^{-ik_{z,j}(z-d_m)} + \tilde{R}_{j|j-1}e^{+ik_{z,j}(z-d_m)}e^{-2ik_{z,j}(d_{j-1}-d_m)}\right] \tag{S21}$$

For $j = m-1$ in equation (S21), namely at the $m-1|m$ interface with $z = d_{m-1}$, one has

$$D_{m|m-1}^- e^{-ik_{z,m-1}(d_{m-1}-d_m)} = A_{m,o}^- e^{-ik_{z,m}(d_{m-1}-d_m)} \cdot S_{m|m-1} \tag{S22}$$

$$S_{m|m-1} = \frac{T_{m|m-1}}{1 - R_{m-1|m}\tilde{R}_{m-1|m-2}e^{2ik_{z,m-1}(d_{m-1}-d_{m-2})}} \tag{S23}$$

where $D_{m|m-1}^-$ is determined by $A_{m,0}^-$ and the transmission at the $m-1|m$ interface. From (S21), one has

$$\prod_{n=j}^{n=m-1} D_{m|n}^- e^{-ik_{z,n}(d_n-d_m)} = \prod_{n=j}^{n=m-1} D_{m|n+1}^- e^{-ik_{z,n+1}(d_n-d_m)} S_{n+1|n} \tag{S24}$$

Especially, $D_{m|m}^- = A_{m,0}^-$. From equation (S24), the unknown parameter $D_{m|j}^-$ in equation (S21) can be determined by

$$D_{m|j}^- e^{-ik_{z,j}(d_j-d_m)} = \tilde{T}_{m|j}^{j<m} \cdot A_{m,o}^- \tag{S25}$$

$$\tilde{T}_{m|j}^{j<m} = \prod_{n=j}^{n=m-1} S_{n+1|n}\, e^{-ik_{z,n+1}(d_{n+1}-d_n)} \tag{S26}$$

where $\tilde{T}_{m|j}^{j<m}$ can be treated as the generalized transmission coefficient from region m to region j ($m > j$).

Part 6: Field in region j from the forward transition radiation at the $m-1|m$ ($j+1 \le m \le N$) interface

By following equation (S9), the forward transition radiation emitted in region m can be transformed to

$$\begin{aligned} TR_m^+ \to region\ m &= B_{m,o}^+ e^{ik_{z,m}(z-d_{m-1})} + AR_{m,o}^- \left[e^{-ik_{z,m}(z-d_{m-1})} + \tilde{R}_{m|m-1} e^{ik_{z,m}(z-d_{m-1})}\right] \\ AR_{m,o}^- &= B_{m,o}^+ M_m \tilde{R}_{m|m+1} e^{2ik_{z,m}(d_m-d_{m-1})} \\ B_{m,o}^+ &= \frac{A_{m,o}^+}{M_m} = \frac{iq}{\omega\varepsilon_0(2\pi)^3} \cdot a_{m-1|m}^+ \end{aligned} \tag{S27}$$

Here we only need to take the part relevant to $AR_{m,o}^-$ in equation (S27) into consideration. In a multi-layered system, the transmitted field in region j ($j < m$) from the forward transition radiation at the $m-1|m$ ($j < m \le N-1$) can be written as

$$TR_m^+ \to region\ j = C_{m|j}^- \left[e^{-ik_{z,j}(z-d_{m-1})} + \tilde{R}_{j|j-1} e^{+ik_{z,j}(z-d_{m-1})} e^{-2ik_{z,j}(d_{j-1}-d_{m-1})}\right] \tag{S28}$$

By performing similar procedure to part 5, we have

$$C_{m|j}^- e^{-ik_{z,j}(d_j-d_{m-1})} = \tilde{T}_{m|j}^{j<m} \cdot AR_{m,o}^- e^{-ik_{z,m}(d_m-d_{m-1})} \tag{S29}$$

where $\tilde{T}_{m|j}^{j<m}$ is determined by equation (S26).

Part 7: Interference of transition radiation from multiple parallel interfaces

The total electric field in region j ($1 \le j \le N+1$) can now be expressed as

$$E_{z,j}^R = \begin{cases} \dfrac{iq}{\omega\varepsilon_0(2\pi)^3} \cdot a_1 \cdot e^{-ik_{z,1}(z-d_1)} & (j=1) \\ \dfrac{iq}{\omega\varepsilon_0(2\pi)^3} \left[a_j^- \cdot e^{-ik_{z,j}(z-d_j)} + a_j^+ \cdot e^{ik_{z,j}(z-d_{j-1})}\right] & (2 \le j \le N) \\ \dfrac{iq}{\omega\varepsilon_0(2\pi)^3} \cdot a_{N+1} \cdot e^{ik_{z,N+1}(z-d_N)} & (j=N+1) \end{cases} \tag{S30}$$

where a_j^+ (a_j^-) represent the generalized forward (backward) radiation factor in region j.

The radiation in region 1 comes solely from all the interfaces below region j ($j = 1$)

$$TR_j^- \to region\ j + \sum_{m=j+1}^{N} TR_m^- \to region\ j + \sum_{m=j+1}^{N} TR_m^+ \to Region\ j \tag{S31}$$

Equation (S31) can be simplified with equations (S20,S21,S27) as stated in parts 4-6.

As an example, the radiation in region 1 originates solely from the interfaces below it, namely $E_{R,1}^+ = 0$ and $a_1^+ = 0$. Then the radiation factor in region 1 can be formulated as

$$E_{z,1}^{R,-} = \frac{iq}{\omega\varepsilon_0(2\pi)^3} a_1^- \cdot e^{-ik_{z,1}(z-d_1)}$$

158 $$a_1 = a_1^- = \frac{\omega\varepsilon_0(2\pi)^3}{iq}\left[A_{1,o}^- + \sum_{m=2}^{N}\left(D_{m|1}^- e^{-ik_{z,1}(d_1-d_m)} + C_{m|1}^- e^{-ik_{z,1}(d_1-d_{m-1})}\right)\right] \quad \text{(S32)}$$

159 By eliminating $D_{m|1}^-$ and $C_{m|1}^-$ with equations (S25,S29), one has

160 $$a_1 = \frac{\omega\varepsilon_0(2\pi)^3}{iq}\left[A_{1,o}^- + \sum_{m=2}^{N}\left(\tilde{T}_{m|1}^{1<m}\cdot A_{m,o}^- + \tilde{T}_{m|1}^{1<m}\cdot AR_{m,o}^- e^{-ik_{z,m}(d_m-d_{m-1})}\right)\right] \quad \text{(S33)}$$

161 Similarly, the radiation in region $N+1$ originates solely from all the interfaces above region j ($j = N+1$)

162 $$TR_j^+ \rightarrow Region\ j + \sum_{m=2}^{j-1} TR_m^+ \rightarrow Region\ j + \sum_{m=2}^{j-1} TR_m^- \rightarrow Region\ j \quad \text{(S34)}$$

163 where the components in equation (S34) are determined by equations (S8,S10,S16) as elaborated in detail
164 in parts 1-3. As an example, when $j = N+1$, no backward-propagating field is generated, i.e., $a_{N+1}^- = 0$.
165 Therefore, by comparing equations (S30,S31), the radiation factor a_{N+1}^+ can be expressed as

166 $$a_{N+1}^+ = \frac{\omega\varepsilon_0(2\pi)^3}{iq}\cdot\left[A_{N+1,0}^+ + \sum_{m=2}^{N}\left(C_{m|N+1}^+ e^{ik_{z,N+1}(d_N-d_{m-1})} + D_{m|N+1}^+ e^{ik_{z,N+1}(d_N-d_m)}\right)\right] \quad \text{(S35)}$$

167 With the aid of equations (S14, S19), we further obtain

168 $$a_{N+1}^+ = \frac{\omega\varepsilon_0(2\pi)^3}{iq}\cdot\left[A_{N+1,0}^+ + \sum_{m=2}^{N}\left(\tilde{T}_{m|N+1}^{N+1>m}\cdot A_{m,0}^+ + \tilde{T}_{m|N+1}^{N+1>m}\cdot BR_{m,o}^+ e^{ik_{z,m}(d_{m-1}-d_m)}\right)\right] \quad \text{(S36)}$$

169 Generally, the radiation factor in region j, ($2 \le j \le N$) has the forward-propagating part a_j^+ and the
170 backward propagating part a_j^-, which are determined by

171 $$\frac{iq}{\omega\varepsilon_0(2\pi)^3}a_j^- = \left[A_{j,o}^- + \sum_{m=j+1}^{N}\left(D_{m|j}^- e^{-ik_{z,j}(d_j-d_m)} + C_{m|j}^- e^{-ik_{z,j}(d_j-d_{m-1})}\right)\right] + \left[A_{j,o}^+ + \sum_{m=2}^{j-1}\left(C_{m|j}^+ e^{ik_{z,j}(d_{j-1}-d_{m-1})} + D_{m|j}^+ e^{ik_{z,j}(d_{j-1}-d_m)}\right)\right]\tilde{R}_{j|j+1}e^{ik_{z,j}(d_j-d_{j-1})} \quad \text{(S37)}$$

172 $$\frac{iq}{\omega\varepsilon_0(2\pi)^3}a_j^- = \left[A_{j,0}^+ + \sum_{m=2}^{j-1}\left(C_{m|j}^+ e^{ik_{z,j}(d_{j-1}-d_{m-1})} + D_{m|j}^+ e^{ik_{z,j}(d_{j-1}-d_m)}\right)\right] + \left[A_{j,o}^- + \sum_{m=j+1}^{N}\left(D_{m|j}^- e^{-ik_{z,j}(d_j-d_m)} + C_{m|j}^- e^{ik_{z,j}(d_j-d_{m-1})}\right)\right]\tilde{R}_{j|j-1}e^{-ik_{z,j}(d_{j-1}-d_j)} \quad \text{(S38)}$$

173 By eliminating $C_{m|j}^+$, $D_{m|j}^+$, $C_{m|j}^-$ and $D_{m|j}^-$, one has

$$\frac{iq}{\omega\varepsilon_0(2\pi)^3}a_j^- = \left[A_{j,o}^- + \sum_{m=j+1}^{N}\left(\tilde{T}_{m|1}^{j<m}\cdot A_{m,o}^- + \tilde{T}_{m|1}^{j<m}\cdot AR_{m,o}^- e^{-ik_{z,m}(d_m-d_{m-1})}\right)\right] + \left[A_{j,o}^+ + \sum_{m=2}^{j-1}\left(\tilde{T}_{m|j}^{j>m}\cdot A_{m,0}^+ + \tilde{T}_{m|j}^{j>m}BR_{m,o}^+\cdot e^{ik_{z,m}(d_{m-1}-d_m)}\right)\right]\tilde{R}_{j|j+1}e^{ik_{z,j}(d_j-d_{j-1})} \tag{S39}$$

$$\frac{iq}{\omega\varepsilon_0(2\pi)^3}a_j^+ = \left[A_{j,0}^+ + \sum_{m=2}^{j-1}\left(\tilde{T}_{m|j}^{j>m}\cdot A_{m,0}^+ + \tilde{T}_{m|j}^{j>m}\cdot BR_{m,o}^+ e^{ik_{z,m}(d_{m-1}-d_m)}\right)\right] + \left[A_{j,o}^- + \sum_{m=j+1}^{N}\left(\tilde{T}_{m|j}^{j<m}\cdot AR_{m,o}^- e^{-ik_{z,m}(d_m-d_{m-1})} + \tilde{T}_{m|j}^{j<m}\cdot A_{m,o}^-\right)\right]\tilde{R}_{j|j-1}e^{-ik_{z,j}(d_{j-1}-d_j)} \tag{S40}$$

S1.3 Angular spectral energy density of interfacial Cherenkov radiation

In this subsection we calculate the angular spectral energy density of interfacial Cherenkov radiation. The backward angular spectral energy density $U_{\mathrm{B}}(\theta, v)$ can be expressed as

$$W_1 = \int_0^{+\infty} d\omega \int_0^{\frac{\pi}{2}} d\theta U_{\mathrm{B}}(\theta, v)\cdot(2\pi\sin\theta) \tag{S41}$$

where the radiation angle θ in this case is the angle between the wavevector $\bar{k}$ and $-\bar{v}$ as illustrated in Fig. 3*A*.

In the top (bottom) region, since the electric energy and magnetic energy are equal in free space. Therefore, it's sufficient to calculate the energy of the radiation field E^R asympthotically as $t\to\infty$, at which the radiated wave train is already at a great distance to the interface and then separated from the charge's intrinsic field. Moreover, if the origin is moved along the axis into the region of the radiated wave-train, the integration with respect to z can be taken from $-\infty$ to $+\infty$. This way

$$W_1 = \varepsilon_1\lim_{t\to\infty}\int d\bar{r}|\bar{E}_1^R(\bar{r},t)|^2 = \varepsilon_1\lim_{t\to\infty}\int d\bar{r}_\perp\int_{-\infty}^{\infty}dz\,|\bar{E}_1^R(\bar{r},t)|^2 \tag{S42}$$

$$|\bar{E}_1^R(\bar{r},t)|^2 = \int d\bar{k}_\perp d\bar{k}'_\perp d\omega d\omega' \bar{E}^R_{\bar{k}_\perp,\omega,1}(z)\bar{E}^R_{\bar{k}'_\perp,\omega',1}{}^*(z)e^{i\left[(\bar{k}_\perp-\bar{k}'_\perp)\cdot\bar{r}_\perp-(\omega-\omega')t\right]} \tag{S43}$$

By substituting equation (S43) into (S42) and integrating over $d\bar{r}_\perp dz d\bar{k}'_\perp d\omega'$ in equation (S42), one has

$$W_1 = 2\int_0^{+\infty}\int \varepsilon_1|a_1|^2\left(\frac{q}{\omega\varepsilon_0(2\pi)^3}\right)^2\frac{\omega^2\sqrt{\varepsilon_{\mathrm{r},1}}}{ck_\perp^2}\sqrt{1-\frac{k_\perp^2c^2}{\omega^2\varepsilon_{\mathrm{r},1}}}(2\pi)^3\,d\bar{k}_\perp d\omega \tag{S44}$$

For all emitted photons, the integration over $d\bar{k}_\perp$ should be taken under the condition of $k_\perp^2 \le \frac{\omega^2}{c^2}\varepsilon_{\mathrm{r},1}$. From equations (S41,S44), backward angular spectral energy density can be obtained as

$$U_{\mathrm{B}}(\theta, v) = \frac{\varepsilon_{\mathrm{r},1}^{3/2} q^2 \cos^2\theta \, |a_1|^2}{4\pi^3 \varepsilon_0 c \sin^2\theta} \tag{S45}$$

By following the identical procedure, the forward angular spectral energy density $U_{\mathrm{F}}(\theta, v)$ can be obtained as

$$U_{\mathrm{F}}(\theta, v) = \frac{\varepsilon_{\mathrm{r},N+1}^{3/2} q^2 \cos^2\theta \, |a_{N+1}|^2}{4\pi^3 \varepsilon_0 c \sin^2\theta} \tag{S46}$$

The radiation angle θ for the forward radiation represents the angle between the wavevector $\bar{k}$ and the electron velocity $\bar{v}$.

The total angular spectral energy density can then be written as $U_{\mathrm{total}} = U_{\mathrm{B}}(\theta, v) + U_{\mathrm{F}}(\theta, v)$.

S1.4 Field distribution of excited interfacial Cherenkov radiation

By following the same procedure as equation (S6), the field distribution of interfacial Chernkov radiation can be written as

$$\begin{gathered}
\bar{E}_z(\bar{r}, t) = \bar{E}_z^q(\bar{r}, t) + \bar{E}_z^R(\bar{r}, t) \\
\bar{E}_{z,j}^q(\bar{r}, t) = \hat{z} \int_{-\infty}^{\infty} d\omega \frac{-q}{8\pi\omega\varepsilon_0\varepsilon_{\mathrm{r},j}} \left(\frac{\omega^2}{c^2}\varepsilon_{\mathrm{r},j} - \frac{\omega^2}{v^2} \right) H_0^{(1)}\left(\rho \sqrt{\frac{\omega^2}{c^2}\varepsilon_{\mathrm{r},j} - \frac{\omega^2}{v^2}} \right) e^{i\frac{\omega}{v}z - \omega t} \\
\bar{E}_{z,j}^R(\bar{r}, t) = \hat{z} \int_{-\infty}^{\infty} d\omega \int_0^{\infty} dk_\perp \frac{iq}{\omega\varepsilon_0 (2\pi)^3} \left(2\pi k_\perp J_0(k_\perp \rho)\right) \left[a_j^- e^{-ik_{z,j}(z - d_j) - i\omega t} + a_j^+ e^{ik_{z,j}(z - d_{j-1}) - i\omega t} \right]
\end{gathered} \tag{S47}$$

where the only unknown radiation factors a_j^- and a_j^+ can be determined in part 7 of the section 1.3.

S1.5 Sommerfeld integration for interfacial Cherenkov radiation

In this subsection, we give some details about the numerical calculation of interfacial Cherenkov radiation by exploiting the Sommerfeld integration. For a given frequency, the poles for guidance modes can be avoided by choosing a proper Sommerfeld path of integration [68,76]. In order to illustrate the group cone in Fig. 2*C*, an additional window function is applied. Correspondingly, the current density is changed to

$$\bar{J}_G^q(\bar{r}, t) = \hat{z} q v \delta(x) \delta(y) \frac{1}{\sigma_z \sqrt{2\pi}} e^{-\frac{(z - vt)^2}{2\sigma_z^2}} \tag{S48}$$

In other words, a Gaussian-shaped electron bunching is utilized to study the Cherenkov radiation [66]. Accordingly, the radiation factor a is changed to $a_G = a e^{-\frac{\sigma_z^2 \omega^2}{2\, v^2}}$, and the window function used in Fig. 2*C*-*D* is $F_{\mathrm{win}}(\omega) = e^{-\frac{(\omega - \omega_0)^2}{2\sigma_\omega^2}}$, where $\sigma_\omega = v/\sigma_z$, and $\sigma_z = 2.5\, \lambda_0$ is chosen.

Section S2: More about Huygens construction for interfacial Cherenkov radiation

S2.1 Connection between Huygens wavelets, ray surfaces and wave-vector surfaces

In this subsection, we analyze the connection between Huygens wavelets, ray surfaces and wave-vector surfaces. Generally, Huygens wavelets have the shape of the ray surface, namely the surface with a constant phase [65] instead of the wave-vector surface (the surface with a constant frequency in $\bar{k}$ space).

For all points at a Huygens wavelet, they have a same phase φ, namely $\varphi = \bar{k} \cdot \bar{r} - \omega t$. Below we let the function $g(\bar{r}, \varphi) = \bar{k} \cdot \bar{r} - \omega t - \varphi$. Then if $g(\bar{r}, \varphi) = 0$, the solution corresponds to the constant-phase surface for Huygens wavelets or the ray surface.

In $\bar{r}$ space, we have $\frac{dg}{d\bar{r}} = \frac{\partial g}{\partial \Phi} \nabla_r \varphi + \nabla_r g = 0$, where $d\bar{r} = d\,\hat{1} + d\hat{z}$. Therefore, we have

$$\nabla_r \varphi = \bar{k} = -\frac{\nabla_r g}{\partial g / \partial \varphi} \tag{S49}$$

Since $\nabla_r g$ in equation (S49) is normal to the ray surface, the wavevector $\bar{k}$ should also be normal to the ray surface, that is,

$$\delta\bar{r} \cdot \bar{k} = 0 \tag{S50}$$

In equation (S50), $\delta\bar{r}$ is a differential element at a specific point on the Huygens wavelet, and it is always parallel to the tangent line of the Huygens wavelet at that point. If $\varphi = \varphi_0$ for the initial phase, we have

$$\bar{k} \cdot \bar{r} = \omega t + \varphi_0 \tag{S51}$$

This way, for given frequency and time, $\delta\bar{r} \cdot \bar{k} + \delta\bar{k} \cdot \bar{r} = 0$. With the knowledge of equation (S50), we further have

$$\delta\bar{k} \cdot \bar{r} = 0 \tag{S52}$$

In equation (S52), $\delta\bar{k}$ is a differential element at specific point on the ray surface, and it is always parallel to the tangent line of the wave-vector surface at that point.

From the above analysis, if the wave-vector surface is given, the shape of ray surface and thus the Huygens wavelets can be determined by equations (S51,S52) as schematically shown in Fig. S2*A*. Similarly, the shape of wave-vector surface can be obtained by using equations (S50,S51), if the ray surface is known as schematically shown in Fig. S2*B*.

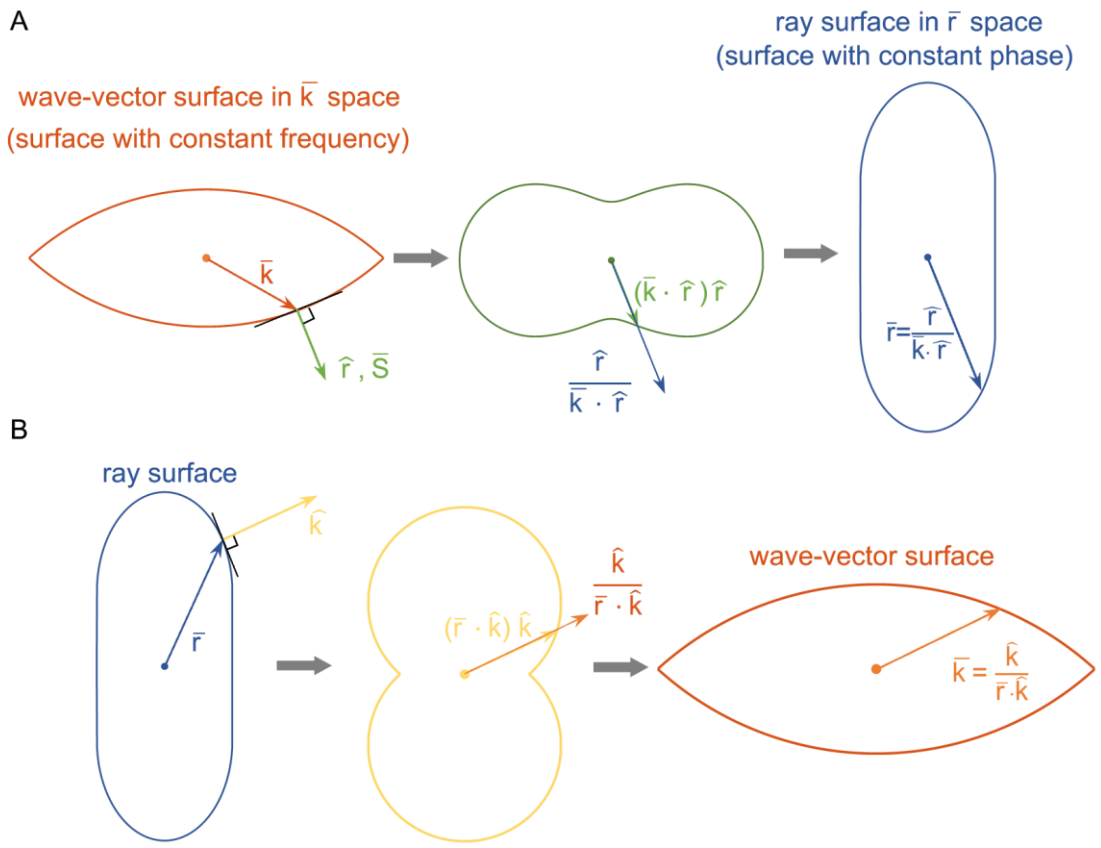

Fig. S2 Wave-vector surface and ray surface for Bloch modes of photonic crystals. The structure of the photonic crystal corresponds to Fig. 2. in the main text. (*A*) Construction of the ray surface if the wave-vector surface is known. (*B*) Construction of the wave-vector surface if the ray surface is known. For the plot in the middle panel of *B*, the result is also known as the phase-velocity surface, since $\bar{v}_{\mathrm{p}} = \hat{k} v_{\mathrm{p}} = \hat{k} \frac{\omega}{k}$.

S2.2 Physical interpretation of ray velocity

In this subsection, we elaborate on the physical meaning of ray velocity.

The velocity $\bar{u} = \bar{r}/t$ along the ray (namely, the ray velocity) plays an important role in the Huygens construction. Physically speaking, the direction of group velocity $\bar{v}_{\mathrm{g}} = \partial\omega/\partial\bar{k}$ is normal to the wave-vector surface, since

$$\delta\bar{k} \cdot \bar{v}_{\mathrm{g}} = 0 \tag{S53}$$

By comparing equations (S52,S53), one can obtain $\bar{v}_{\mathrm{g}} \parallel \bar{r} \parallel \bar{u}$. That is, the energy flow is directed along the ray, and the group velocity is parallel to the ray velocity.

Now consider a Huygens source at the origin O of a selected coordinate in $\bar{r}$ space with an initial phase $\varphi = 0$. Then after time t, $\varphi = \bar{k} \cdot \bar{r} - \omega t$. This way, we have

$$\hat{k} \cdot \bar{u} = v_{\mathrm{p}} \tag{S54}$$

From equation (S54), the magnitude of ray velocity can be obtained.

S2.3 Ray velocity and group velocity

In this subsection, we consider the relationship between the ray velocity and the group velocity. For time-harmonic fields, we have $\bar{E}(\bar{r},t) = \mathrm{Re}\left[\bar{E}e^{-i\omega t}\right]$. According to Ginzburg's deviation [77] of group velocity in dispersive non-magnetic media with negligible loss, we have

$$\bar{v}_{\mathrm{g}} = \frac{\partial\omega}{\partial\bar{k}} = \frac{\langle\bar{S}(\bar{r},t)\rangle}{\langle W_T\rangle} = \frac{\frac{1}{4}\left(\bar{E}\times\bar{H}^* + \bar{E}^*\times\bar{H} - \omega\bar{E}^*\cdot\frac{\partial\bar{\bar{\varepsilon}}}{\partial\bar{k}}\cdot\bar{E}\right)}{\frac{1}{4}\left[\bar{E}\cdot\frac{\partial(\omega\bar{\bar{\varepsilon}})}{\partial\omega}\cdot\bar{E}^* + \mu|\bar{H}|^2\right]} \tag{S55}$$

where $\bar{\bar{\varepsilon}}$ is the anisotropic permittivity and $\mu = \mu_0$ is the permeability of free space, $\langle\bar{S}(\bar{r},t)\rangle = \frac{1}{4}\left(\bar{E}\times\bar{H}^* + \bar{E}^*\times\bar{H} - \omega\bar{E}\cdot\frac{d\bar{\bar{\varepsilon}}}{d\bar{k}}\cdot\bar{E}^*\right)$ is the time-average Poynting power density, $\langle W_T\rangle = \frac{1}{4}\left[\bar{E}\cdot\frac{d(\omega\bar{\bar{\varepsilon}})}{d\omega}\cdot\bar{E}^* + \mu|\bar{H}|^2\right]$ is the time-average total electromagnetic field energy density [77,78].

From equation (S55), one has

$$\begin{aligned}
\hat{k}\cdot\bar{v}_{\mathrm{g}} &= \frac{\bar{k}}{k}\cdot\frac{\frac{1}{4}\left(\bar{E}\times\bar{H}^* + \bar{E}^*\times\bar{H} - \omega\bar{E}^*\cdot\frac{\partial\bar{\bar{\varepsilon}}}{\partial\bar{k}}\cdot\bar{E}\right)}{\frac{1}{4}\left[\bar{E}\cdot\frac{\partial(\omega\bar{\bar{\varepsilon}})}{\partial\omega}\cdot\bar{E}^* + \mu|\bar{H}|^2\right]} \\
&= \frac{\left[-\bar{E}\cdot\left(\bar{k}\times\bar{H}^*\right) + \bar{H}^*\cdot\left(\bar{k}\times\bar{E}\right)\right] - \bar{k}\cdot\left(\omega\bar{E}^*\cdot\frac{\partial\bar{\bar{\varepsilon}}}{\partial\bar{k}}\cdot\bar{E}\right)}{k\left[\bar{E}\cdot\frac{\partial(\omega\bar{\bar{\varepsilon}})}{\partial\omega}\cdot\bar{E}^* + \mu|\bar{H}|^2\right]} \\
&= v_{\mathrm{p}}\cdot\frac{\left[\bar{E}\cdot\bar{\bar{\varepsilon}}^*\cdot\bar{E}^* + \mu|\bar{H}|^2 - \bar{k}\cdot\left(\omega\bar{E}^*\cdot\frac{\partial\bar{\bar{\varepsilon}}}{\partial\bar{k}}\cdot\bar{E}\right)\right]}{\left[\bar{E}\cdot\frac{\partial(\omega\bar{\bar{\varepsilon}})}{\partial\omega}\cdot\bar{E}^* + \mu|\bar{H}|^2\right]}
\end{aligned} \tag{S56}$$

If the spatial and temporal dispersion is negligible, one has $\frac{d(\omega\bar{\bar{\varepsilon}})}{d\omega} = \bar{\bar{\varepsilon}}$ and $\frac{d\bar{\bar{\varepsilon}}}{d\bar{k}} = 0$. By applying these to equation (S56), one has

$$\hat{k}\cdot\bar{v}_{\mathrm{g}} = v_{\mathrm{p}} \tag{S57}$$

From equations (S54,S56), the magnitudes of the ray velocity and the group velocity are not equal in presence of spatial or temporal dispersion, namely $\left|\bar{v}_{\mathrm{g}}\right| \neq |\bar{u}|$. In other words, we have $\left|\bar{v}_{\mathrm{g}}\right| = |\bar{u}|$ only in non-dispersive medium.

Section S3: Aperture of group cone for the interfacial Cherenkov radiation

In this section, we study the aperture of the group cone. Similarly, for a wave-vector surface determined by $f(\bar{k}, \omega) = 0$, we have

$$\bar{v}_{\mathrm{g}} = \nabla_k \omega = -\frac{\nabla_k f}{\partial f / \partial \omega} \tag{S58}$$

Therefore, the group velocity $\bar{v}_{\mathrm{g}}$ for an excited Bloch mode with a wavevector $\bar{k}$ can be directly determined from equation (S58).

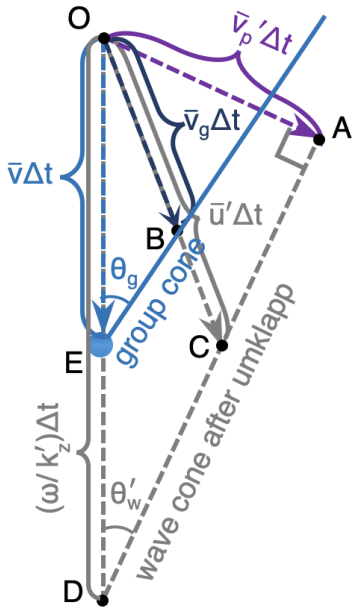

Fig. S3. Wave cone after umklapp scattering and group cone. The parameters with a prime in the superscript indicate that they undergo the umklapp scattering.

The aperture θ_{g} of the group cone as schematically shown in Fig. S3 is given by [24,62,67]

$$\tan\theta_{\mathrm{g}} = \frac{v_{\mathrm{g},\perp}}{v - v_{\mathrm{g},z}} \tag{S59}$$

where $\bar{v}_g = \hat{1}\, v_{\mathrm{g},\perp} + \hat{z} v_{\mathrm{g},z}$. Equation (S59) indicates that the aperture of the group cone is related to group velocity. Similarly, from Fig. S3, the aperture of the wave cone after the umklapp scattering can be determined by

$$\tan\theta_{\mathrm{w}}' = \frac{u_{\perp}'}{v_{\mathrm{apex,w}}' - u_z'} \text{ or } \sin\theta_{\mathrm{w}}' = \frac{v_{\mathrm{p}}'}{v_{\mathrm{apex,w}}'} \tag{S60}$$

where $\bar{u} = \hat{1}\, u_{\perp}' + \hat{z} u_z'$. Equation (S60) indicates that the aperture of the reshaped wave cone after the umklapp scattering is related to the ray velocity or the phase velocity.

Section S4: Correspondence between radiation angle and electron velocity

In this section, we obtain the correspondence between the electron velocity and the radiation angle of interfacial Cherenkov radiation. For Bloch-modes inside our designed 1D photonic crystal in Fig. 1, the wave-vector surface $f(k_\perp, k_z, \omega) = 0$ is determined by

$$f(k_\perp, k_z, \omega) = \cos(k_z d) - \left[\cos k_{z,1} d_1 \cos k_{z,2} d_2 - \frac{1}{2}\sin(k_{z,1} d_1)\sin(k_{z,2} d_2)\left(\frac{\varepsilon_{r,1} k_{z,2}}{\varepsilon_{r,2} k_{z,1}} + \frac{\varepsilon_{r,2} k_{z,1}}{\varepsilon_{r,1} k_{z,2}}\right)\right] \quad \text{(S61)}$$

where $d = d_1 + d_2$ is the unit-cell thickness of photonic crystals, d_j is the thickness of the photonic-crystal constituent with $\varepsilon_{r,j}$, $k_{z,j} = k_0\sqrt{\varepsilon_{r,j} - \sin^2\theta}$, and j is either 1 or 2.

By enforcing the phase matching condition between the moving electron and the excited Bloch modes, in z direction we have $k_z = \frac{\omega}{v}$. From the definition of radiation angle in the main text or Fig. 3, we have $k_\perp = \frac{\omega}{c}\sin\theta$. By applying $k_z = \frac{\omega}{v}$ and $k_\perp = \frac{\omega}{c}\sin\theta$ into the wave-vector surface, we have

$$f\left(\frac{\omega}{c}\sin\theta, \frac{\omega}{v}, \omega\right) = 0 \quad \text{(S62)}$$

By combining equations (S61-S62), one can directly obtain the correspondence between the radiation angle and the electron velocity.

Section S5: More discussion on the interfacial Cherenkov radiation

S5.1 Influence of the variations of material's permittivity and the thickness of the constituent dielectric layer on the interfacial Cherenkov radiation

In this subsection, we show in Figs. S4-S5 that the revealed interfacial Cherenkov radiation has a certain degree of tolerance to both the variation of material's permitivity and the variation of thickness of each layer for the designed photonic crystal. These tolerances may facilitate the fabrication of samples for future experimental demonstration.

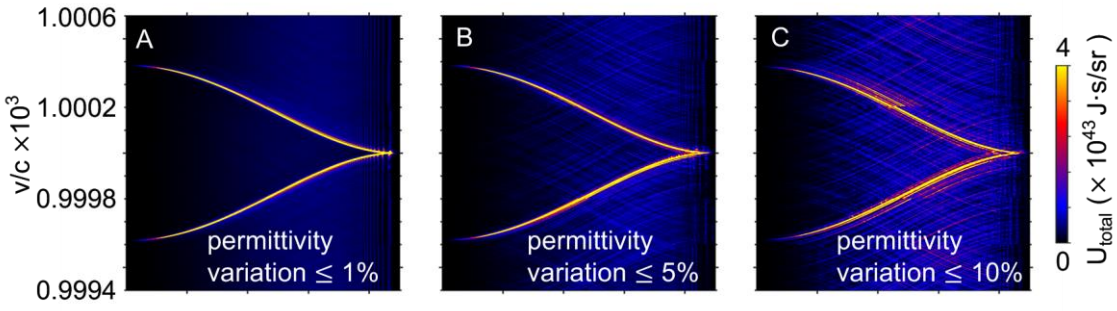

Fig. S4. Influence of the variation of material's permitivity on the interfacial Cherenkov radiation. For illustration, here the photonic crystal is identical to that in Fig. 3*D*, except that each layer in the designed

photonic crystal has random variation on material's permitivity. The maximal variation of material's permitivity in (*A*-*C*) are 1%, 5% and 10%, respectively.

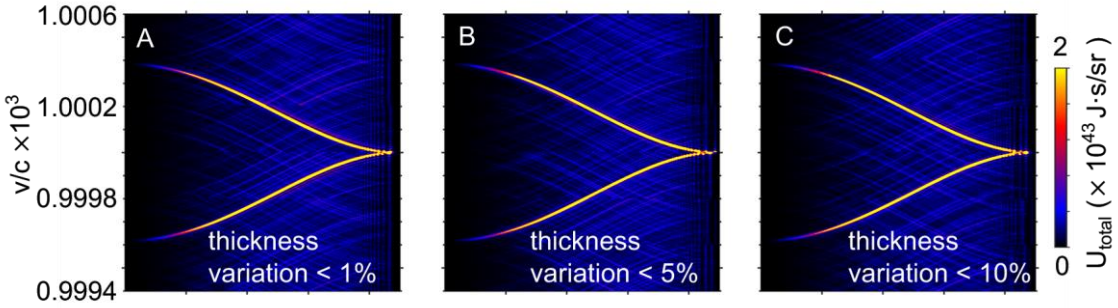

Fig. S5. Influence of the variation of thickness of the constituent dielectric slab on the interfacial Cherenkov radiation. For illustration, here the photonic crystal is identical to that in Fig. 3*D*, except that each layer in half of all unit cells of the designed photonic crystal has random variation on the thickness. The maximal variation of thickness of the constituent slab in (*A*-*C*) are 1%, 5% and 10%, respectively.

S5.2 Influence of material loss on the interfacial Cherenkov radiation

In this subsection, we study the influence of material loss on the interfacial Cherenkov radiation. Actually, there are abundant choices of lossless dielectrics in practice [11,79-81], and hence, there is in principle no need to consider material loss in the design of photonic crystals. Nevertheless, we investigate in Fig. S6 the influence of material loss on the interfacial Cherenkov radiation. Fig. S6 shows that the interfacial Cherenkov radiation would emerge if the material loss is reasonably large (e.g. $\mathrm{Im}(\varepsilon_{\mathrm{r},1}) \leq 0.01$).

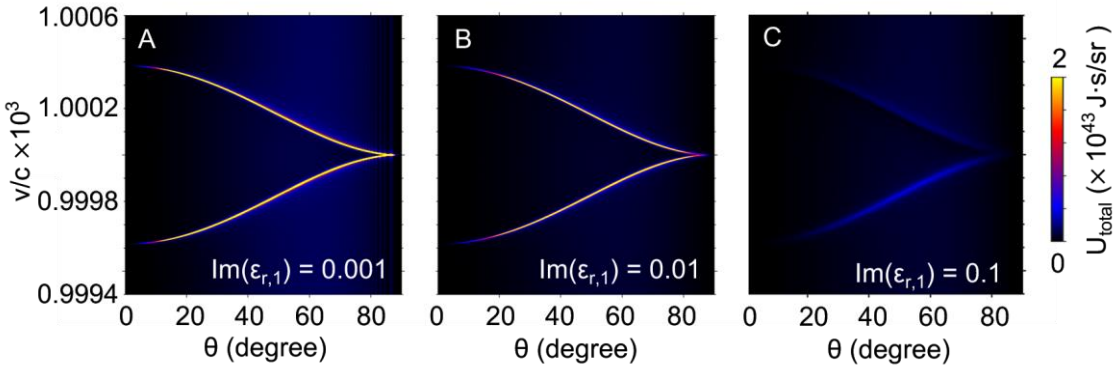

Fig. S6. Influence of material loss on the interfacial Cherenkov radiation. The photonic crystal is identical to that in Fig. 3, except for the material loss. To be specific, the relative partitivities of the two constituent materials for the designed photonic crystal are set to be $\varepsilon_{\mathrm{r},1} = 2.1 + i \cdot \mathrm{Im}(\varepsilon_{\mathrm{r},1})$ and $\varepsilon_{\mathrm{r},2} = 2.3$, respectively. The value of $\mathrm{Im}(\varepsilon_{\mathrm{r},1})$ is given in each plot, and we have $\mathrm{Im}(\varepsilon_{\mathrm{r},1}) = 0$ in Fig. 3. With the increase of $\mathrm{Im}(\varepsilon_{\mathrm{r},1})$, the interfacial Cherenkov radiation may still emerge, but with degraded intensity and directionality.

S5.3 Correlations between the order of umklapp scattering and the photon exaction efficiency of interfacial Cherenkov radiation

In this subsection, we show in Fig. S7 that the photon extraction efficiency $\eta(\omega) = \frac{w(\omega)}{(\hbar\omega)E_{\mathrm{k}}}$ of interfacial Cherenkov radiation exhibits a periodic oscillation tendency with respect to the order of umklapp scattering or the electron velocity. Such a tendency arises from the fact that both the radiation spectrum $w(\omega)$ and the electron's kinetic energy E_{k} have a similar decreasing tendency when the electron velocity decreases (or when the order of umklapp scattering increases); moreover, the radiation spectrum would locally oscillate with respect to the electron velocity or the order of umklapp scattering, since the interfacial Cherenkov radiation results from the constructive interference of transition radiation from many parallel interfaces.

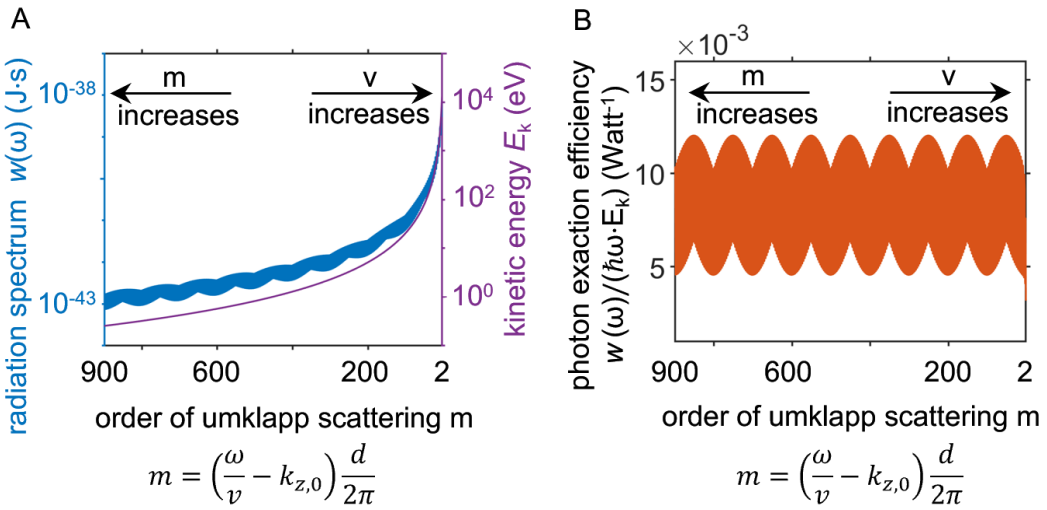

Fig. S7. Correlation between the photon exaction efficiency of interfacial Cherenkov radiation and the order of umklapp scattering m or the electron velocity v. The intricate relationship between the electron velocity and the order of umklapp scattering is determined by the phase matching condition of $\frac{\omega}{v} = k_{z,0} + m \cdot \frac{2\pi}{d}$, where $k_{z,0} \in (-\pi/d, \pi/d)$ is the z-component wavevector of emitted light within the first Brillouin zone after the umklapp scattering. For illustration, we set $k_{z,0} = 0.28\ k_0$ in this figure; under this scenario, the component of wavevector parallel to the interface is $k_{\perp} = 0.55\ k_0$. All the parameters are the same as those in Fig. 3. (*A*) Radiation spectrum $w(\omega)$ as a function of the order of umklapp scattering m or the electron velocity v. (*B*) Photon extraction efficiency of interfacial Cherenkov radiation as a function of the order of umklapp scattering m or the electron velocity v. The photon extraction efficiency exhibits a periodic oscillation tendency with respect to the order of umklapp scattering or the electron velocity.

S5.4 More cases of interfacial Cherenkov radiation from ultralow-energy electrons

In Figs. 3-4, we provide the cases of interfacial Cherenkov radiation from low-energy electrons with their kinetic energy being around 100 eV. These electrons are feasible by using a commercial electron accelerator (e.g. *Model #: ELG-2 EGPS-1022*) or other customed electron guns [82]. In principle, interfacial Cherenkov radiation could occur for any electron velocity, for example, even when the electron velocity is down to the order of $10^{-3}c$ in Figs. S8-S9. These ultralow-energy electrons are also achievable in practice. For example, the kinetic energy of electrons in Low Energy Electron Microscope (LEEM) [83-85] could fall within the range of [0,100] eV. Meanwhile, for the case of $v/c \leq 10^{-3}$, we may use other heavier charged particles (e.g., protons) instead of electrons for the creation of interfacial Cherenkov radiation. For example, a compact proton source with a velocity down to $10^{-4}c$ was reported in recent experiments [86].

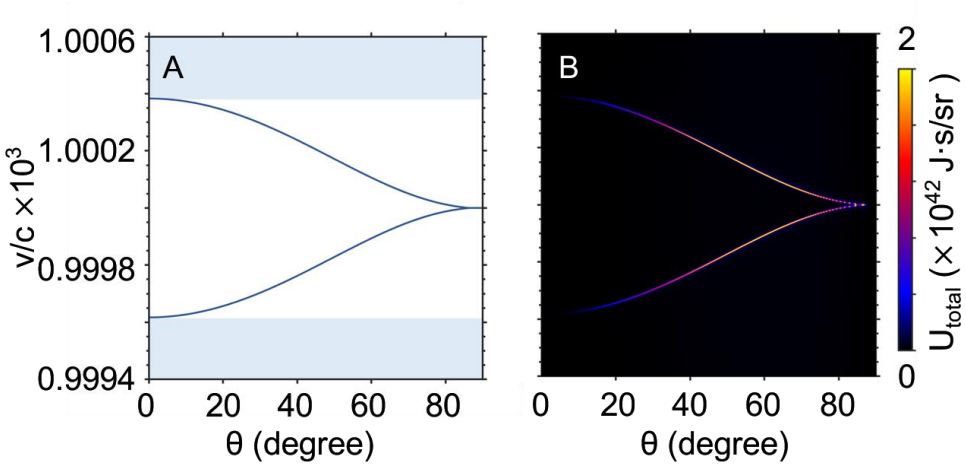

Fig. S8. Interfacial Cherenkov radiation from ultralow-energy electron perpendicularly penetrating through a photonic crystal with a finite thickness. The structural setup of the photonic crystal is the same as that in Fig. 3. The velocity range of $v/c \in [0.9994,1.0006] \times 10^{-2}$ corresponds to the electron kinetic energy of $E_{\mathrm{k}} \in [0.2552, 0.2558]$ eV. (*A*) Relation between the radiation angle of interfacial Cherenkov radiation and the electron velocity. (*B*) $U_{\mathrm{total}} = U_{\mathrm{B}}(\theta, v) + U_{\mathrm{F}}(\theta, v)$ as a function of the electron velocity and the radiation angle, where $U_{\mathrm{F}}(\theta, v)$ and $U_{\mathrm{B}}(\theta, v)$ represent the angular spectral energy densities of the forward and backward radiation, respectively.

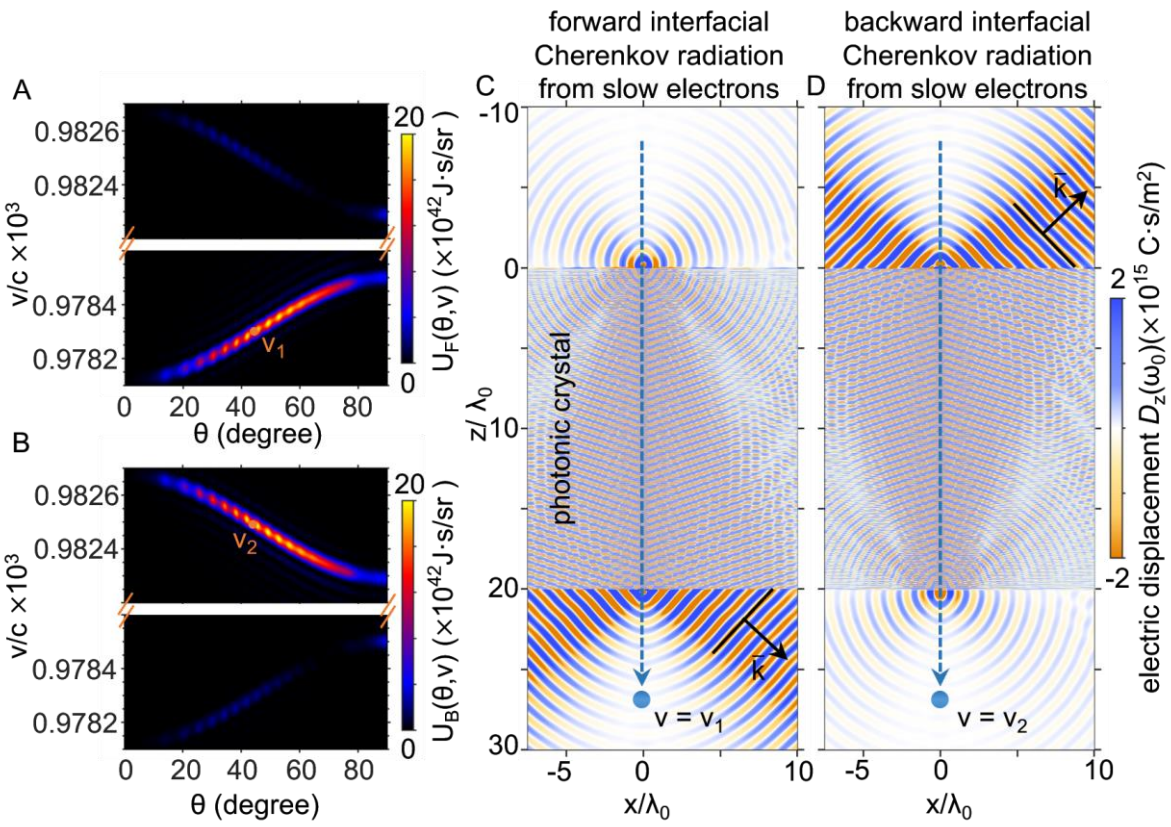

Fig. S9. Forward and backward interfacial Cherenkov radiation excited by low-energy electrons from a photonic crystal with a finite thickness. The structural setup of the photonic crystal is $d_1 = d_2 = 0.05\lambda_0$, $\varepsilon_{r,1} = 2.1$, and $\varepsilon_{r,2} = 8.9$. (*A*) Angular spectral energy density $U_F(\theta, v)$ of the forward free-electron radiation. (*B*) Angular spectral energy density $U_B(\theta, v)$ of the backward free-electron radiation. (*C*) Effective forward interfacial Cherenkov radiation, under the condition that the electron velocity is $v = v_1$, whose corresponding kinetic energy is $E_{k,1} = 0.245$ eV. (*D*) Effective backward interfacial Cherenkov radiation under the condition that the electron velocity is $v = v_2$,whose corresponding kinetic energy is $E_{k,1} = 0.247$ eV.

S5.5 Discussion on the quantum recoil effect

The quantum recoil effect was firstly formulated by Ginzburg in 1940 [48,87,88] and would affect the electron kinetic energy. For conceptual demonstration, we mainly consider the case of $\frac{\hbar\omega}{E_k} \ll 1$ (namely the emitted photon energy $\hbar\omega$ is much smaller than the electron kinetic energy E_k) in this work so that the related quantum recoil effect can be reasonably neglected. For example, since the kinetic energy of electrons in Fig. 3 is around 100 eV, the working wavelength in free space in Fig. 3 can be for example 5 μm, whose

corresponding photon energy is 0.25 eV. As another example, since the kinetic energy of electrons is around 0.26 eV in Fig. S8, the working wavelength in free space in Fig. S8 can be for example 500 μm, whose corresponding photon energy is 2.48 meV. Meanwhile, because of the ultralow radiation efficiency (down to 10^{-10}) as shown in Fig. S10, the total energy of emitted photons is only a very small fraction of the electron's kinetic energy. This way, it is reasonable to assume that the electron velocity remains almost unchanged during its penetration through the designed sample. In short, our theory is formulated far from the quantum regime where the classical electromagnetic wave theory is good enough to predict the light emission.

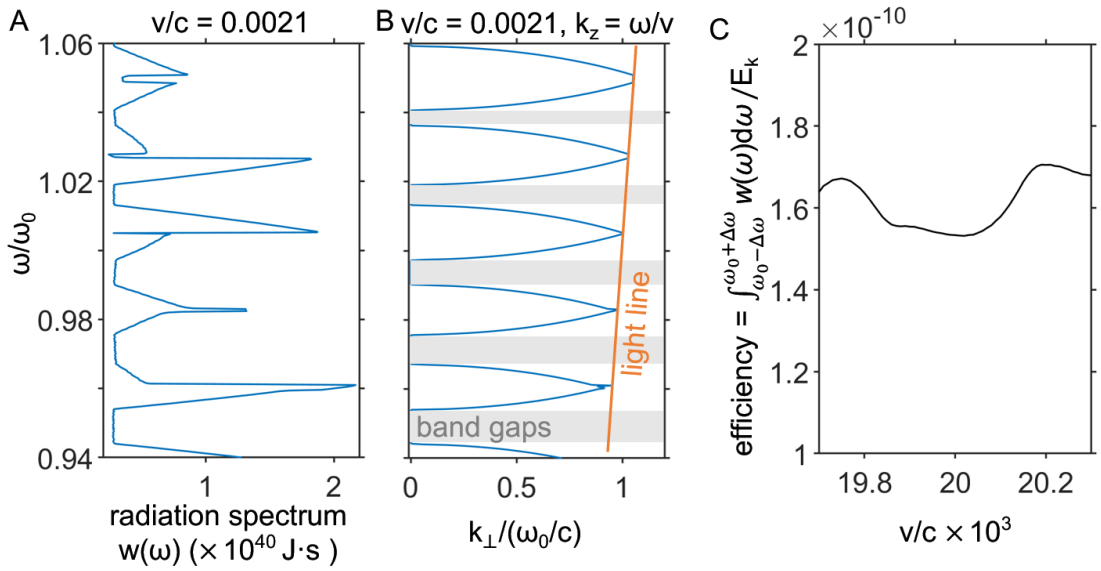

Fig. S10. Radiation efficiency of the interfacial Cherenkov radiation. The photonic crystal is the same as that in our updated Fig. 3 in the main text. (*A*) Radiation spectrum $w(\omega)$. (*B*) Band structures of the designed photonic crystal with a fixed $k_z = \omega/v$. (*C*) Radiation Efficiency as a function of the electron velocity. Mathematically, the radiation efficiency is defined as $\int_{\omega_0-\Delta\omega}^{\omega_0+\Delta\omega} w(\omega)d\omega\,/E_{\mathrm{k}}$. For illustration, $\omega_0/2\pi = 60$ THz is the central working frequency, and $2(\Delta\omega/2\pi) = 7.2$ THz is the considered working bandwidth. In (*A*-*B*), the electron velocity is $v = 0.0201c$, whose corresponding kinetic energy is $E_{\mathrm{k}} = 103$ eV, and the radiation efficiency is around 1.6×10^{-10}. Due to the ultralow value of the radiation efficiency, the electron's velocity can be considered constant during electron's propagation.

S5.6 Influence of electron's energy bandwidth on the interfacial Cherenkov radiation

In this subsection, we study the influence of electron's energy bandwidth on the interfacial Cherenkov radiation. We show in Fig. S11 that the existence of energy bandwidth of free electrons would lead to an

angular spread of interfacial Cherenkov radiation. For example, when the relative energy bandwidth is around 10^{-3} [89,90], the angular spread of interfacial Cherenkov radiation could be around 4° in Fig. S11.

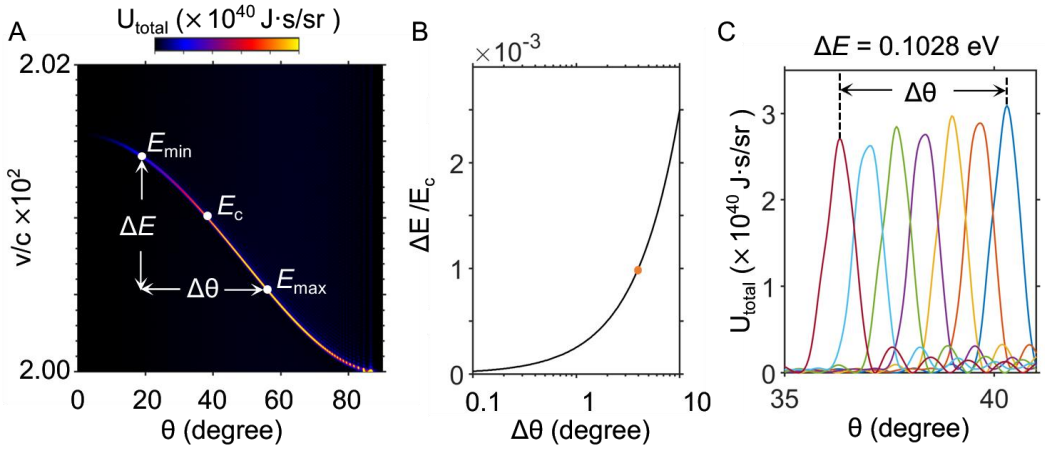

Fig. S11. Influence of the energy bandwidth of free electrons on the interfacial Cherenkov radiation. The photonic crystal is the same as that in Fig. 3. For illustration, the central electron velocity is $v = 0.0201c$, whose corresponding kinetic energy is $E_c = 103$ eV. (*A*) Illustration of the energy bandwidth ΔE of free electrons and the angular spread $\Delta\theta$ of interfacial Cherenkov radiation in the plot of angular spectral energy density of total free-electron radiation. (*B*) Dependence of angular spread $\Delta\theta$ of interfacial Cherenkov radiation on the relative energy bandwidth $\Delta E/E_c$. (*C*) Angular spectral energy density excited by free electrons with different kinetic energies. The corresponding kinetic energy of electrons in (*C*) is $E_k \in [E_{min}, E_{max}]$, where $\Delta E = E_{max} - E_{min}$ and $\Delta E/E_c = 10^{-3}$. Under this scenario, the corresponding angular spread is around 4°.

S5.7 Integration and scalability of interfacial-Cherenkov-radiation-based light sources with enhanced photon exaction efficiency

Regarding the efficiency, we show in Fig. S12 that the photon exaction efficiency [26,70] of interfacial Cherenkov radiation from a photonic crystal could be orders of magnitude enhanced than that of conventional transition radiation from a dielectric slab. Regarding the integration, the interfacial Cherenkov radiation demonstrates nice compatibility with existing techniques for on-chip light sources as schematically shown in Fig. S13*A*-*B*. To be specific, we conceptually show the possibility to integrate the electron emitter directly with the photonic crystal in Fig. S13*B* to create the interfacial Cherenkov radiation. Regarding the scalability, we schematically show in Fig. S13*C* that the interfacial-Cherenkov-radiation-based light sources

may be readily expanded into an array configuration, allowing for their utilization in large-scale photonic devices.

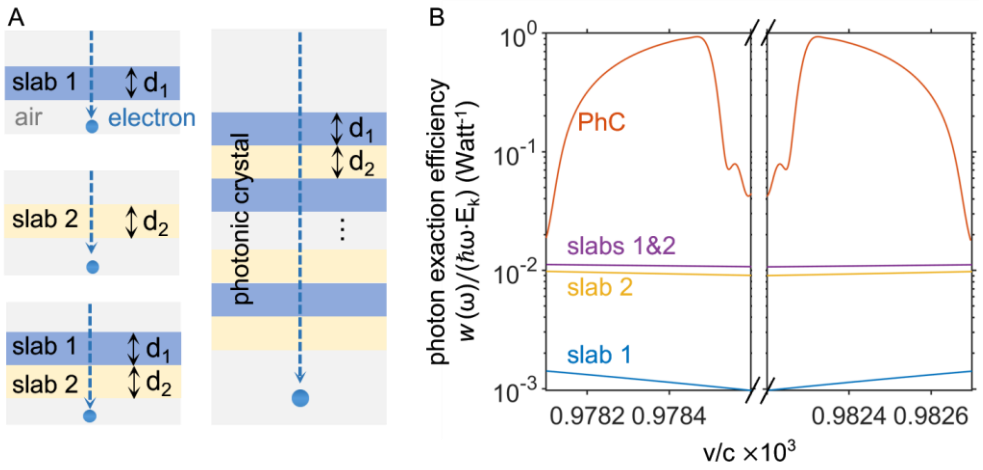

Fig. S12. Comparison of photon exaction efficiency between the interfacial Cherenkov radiation from a photonic crystals (PhC) and the transition radiation from a dielectric slab. The structural setup of photonic crystals is the same as that of Fig. 4, which has 200 unit cells in total. The photon exaction efficiency is defined as $\eta(\omega) = \frac{w(\omega)}{(\hbar\omega)E_{\mathrm{k}}}$ [26,70], where $\hbar\omega$ is the photon energy of emitted light, E_{k} is the electron kinetic energy, and $w(\omega) = \frac{dW}{d\omega} = \int_0^{\pi/2} d\theta\, U_{\mathrm{total}}(\theta, v) \cdot (2\pi \sin\theta)$ is the total radiation spectrum. (*A*) Structural schematic of interfacial Cherenkov radiation from a photonic crystal and conventional transition radiation from the dielectric slab. For illustration, the chosen dielectric is the constituent material of the photonic crystal, and its thickness is the same as each corresponding layer of the photonic crystal. (*B*) Comparison of photon extraction efficiency. The photon exaction efficiency of interfacial Cherenkov radiation could be orders of magnitude enhanced compared to that of conventional transition radiation from a dielectric slab.

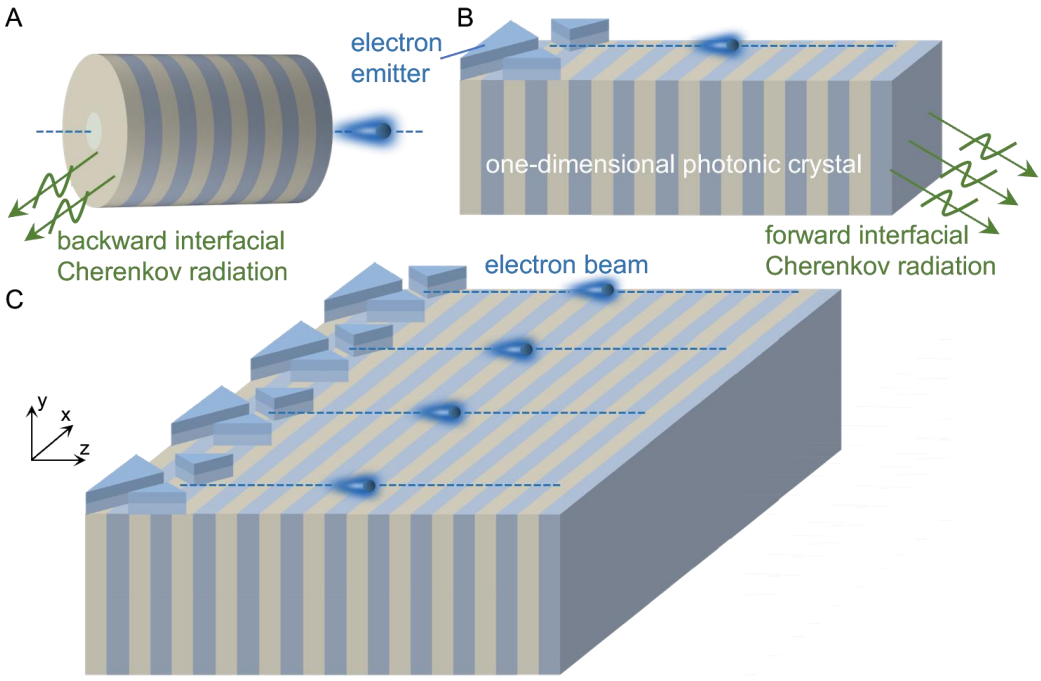

Fig. S13. Conceptual illustration of integrated interfacial-Cherenkov-radiation-based light sources. (*A*-*B*) Structrual schematic of interfacial Cherenkov radiation from low-energy electrons. For the safe penetration of low-energy electrons through the designed photonic crystal, a small hole can be drilled along electron's trajectory as shown in (*A*) [14,91]. For better integration, we may integrate the electron emitter directly on one side wall (parallel to *x*-*z* plane) of the photonic crystal in (*B*) so that the electrons can move along the direction of periodicity with a very small vertical distance to the photonic crystal [16]. For the scheme in (*B*), the electron can safely penetrate throgh the designed photonic crystal, and their induced evenescent waves can have very strong interaction with the beneath photonic crystal. (*C*) An array of integrated interfacial-Cherenkov-radiation-based light sources.

References

[76] Chew, W. *Waves and fields in inhomogeneous media*. (Springer, 1990).
[77] Ginzburg, V. L. *The propagation of electromagnetic waves in plasmas*. (Pergamon Press, 1964).
[78] Musha, T. Electrodynamics of anisotropic media with space and time dispersion. *Proceedings of the IEEE* **60**, 1475-1485 (1972).
[79] Palik, E. D. *Handbook of optical constants of solids*. (Academic press, 1998).
[80] Roques-Carmes, C. *et al.* Towards integrated tunable all-silicon free-electron light sources. *Nat. Commun.* **10**, 3176 (2019)
[81] Shen, Y. *et al.* Optical broadband angular selectivity. *Science* **343**, 1499-1501 (2014).
[82] Matsumoto, Y. *et al.* Development of a low energy small electron gun to study electron transport in hydrogen negative ion source plasmas. *Review of Scientific Instruments* **91**, 013333 (2020).
[83] Neu, P. S., Geelen, D., Thete, A., Tromp, R. M. & van der Molen, S. J. Complementary LEEM and eV-TEM for imaging and spectroscopy. *Ultramicroscopy* **222**, 113199 (2021).
[84] Spence, J. C. H. & Hawkes Peter, W. *Springer handbook of microscopy*. (Springer, 2019).

[85] Geelen, D. *et al.* eV-TEM: Transmission electron microscopy in a low energy cathode lens instrument. *Ultramicroscopy* **159**, 482-487 (2015).
[86] Weiser, A. *et al.* A compact low energy proton source. *arXiv:2306.09003* (2023).
[87] Ginzburg, V. L. Quantum theory of radiation of electron uniformly moving in medium. *Zh. Eksp. Teor. Fiz* **10**, 589 (1940).
[88] Ginzburg, V. L. Radiation by uniformly moving sources (Vavilov-Cherenkov effect, transition radiation, and other phenomena). *Physics-Uspekhi* **39**, 973 (1996).
[89] Krivanek, O. L. et al. Progress in ultrahigh energy resolution EELS. *Ultramicroscopy* **203**, 60-67 (2019).
[90] Tromp, R. M., Hannon, J. B. & Dyck, M. L. Gun energy filter for a low energy electron microscope. *Ultramicroscopy* **253**, 113798 (2023).
[91] Jelley, J. V. *Cerenkov radiation and its applications*. (Pergamon Press, 1958).